Title

Clonal spreading of tumor-infiltrating T cells underlies the robust antitumor immune responses

Authors and Affiliations:

Hiroyasu Aoki[1,2,4], Mikiya Tsunoda[1], Haru Ogiwara[1], Haruka Shimizu[1], Haruka Abe[1], Takaya Abe[3], Shigeyuki Shichino[1], Kouji Matsushima[1], Satoshi Ueha[1,4,5,*]

[1]Division of Molecular Regulation of Inflammatory and Immune Diseases, Research Institute for Biomedical Sciences, Tokyo University of Science, Noda city, Chiba, 278-8510, Japan

[2]Department of Hygiene; Graduate School of Medicine, The University of Tokyo, Bunkyo-ku, Tokyo, 113-0033, Japan

[3]Laboratory for Animal Resources and Genetic Engineering, RIKEN Center for Biosystems Dynamics Research, Chuo-ku, Kobe, Hyogo, 650-0047, Japan

[4]These authors contributed equally

[5]Lead Contact

*Correspondence: ueha@rs.tus.ac.jp

Summary

The repertoire of tumor-infiltrating T cells is an emerging perspective for characterizing effective antitumor T-cell responses. Oligoclonal expansion of tumor T-cell repertoire has been evaluated; however, their association with antitumor effects is unclear. We demonstrated that the polyclonal fraction of the tumor-reactive T-cell repertoire consisting of relatively minor clones increased in tumor-bearing mice treated with anti-PD-L1 or anti-CD4 monoclonal antibody, which was correlated with antitumor effect. Meanwhile, the size of the oligoclonal fraction consisting of major clones remained unchanged. Moreover, the polyclonal fraction was enriched in progenitor exhausted T cells, which are essential for a durable antitumor response, and was more dependent on $CCR7^{+}$ migratory dendritic cells, which are responsible for priming tumor-reactive T cells in the tumor-draining lymph nodes. These results suggest that the expansion of diverse tumor-reactive clones ("clonal spreading") is an important mechanism by which anti-PD-L1 and anti-CD4 treatments induce robust and durable antitumor T-cell responses.

Keywords: TCR repertoire**,** tumor-infiltrating T cells, dLN-tumor overlap, polyclonal fraction, clonal spreading, anti-PD-L1 mAb, anti-CD4 mAb, progenitor exhausted T cells,

37 migratory DC

38

Introduction

Immune checkpoint inhibitors (ICIs), including programmed cell death-1 (PD-1) inhibitors, are widely used to treat various types of cancer. However, only 20%–30% of patients respond to ICIs (Ribas and Wolchok, 2018), and the factors determining the differences between responders and non-responders remain unknown. The differences in clinical responses are not only due to the immune resistance mechanism of the tumor but also due to the strength of the antitumor immune response induced by ICIs (Havel, Chowell, and Chan, 2019). Hence, characterizing the antitumor immune response that leads to better clinical outcomes is critical for optimizing patient selection and developing new therapeutic combinations.

$CD8^+$ tumor-infiltrating T-lymphocytes (TILs), the primary effector cells of the antitumor immune response, are composed of various T-cell clones with different antigen specificities determined by T-cell receptors (TCRs) (Gros et al., 2014; Oliveira et al., 2021; Pasetto et al., 2016). TCR transgenic mice (Overwijk et al., 2003) and peptide-major histocompatibility complex (MHC) multimer technology (Ahmadzadeh et al., 2009) have been used in several pre-clinical and clinical studies to analyze the characteristics of a small set of clones with high affinity to tumor antigens. More recently, TCR sequencing, a global analysis of TCRs using next-generation sequencing,

57 has enabled the analysis of a collection of T-cell clones and the TCR repertoire (Aversa
58 et al., 2020; Kidman et al., 2020). Hence, the TCR repertoire has been used to
59 investigate the features of antitumor T-cell responses, leading to better therapeutic
60 effects.

61 The TCR repertoire of TILs is highly skewed toward a small number of clones,
62 in which the top 1% of the most abundant clones result in more than 20% of the TILs,
63 suggesting the expansion of tumor-reactive clones (Casarrubios et al., 2021; Zhang et
64 al., 2020). Thus, the features of the TCR repertoire of TILs have been evaluated using
65 the clonality index (Chiffelle et al., 2020), representing the extent to which a part of the
66 T-cell clones expanded in the repertoire ("clonal skewing"). Indeed, a higher clonality is
67 associated with antitumor effects (Dovedi et al., 2017; Riaz et al., 2017; Yusko et al.,
68 2019; Zhang et al., 2020). T-cell clones that encounter antigens and proliferate in tumors
69 differentiate into a dysfunctional state called exhaustion (van der Leun et al., 2020; Li et
70 al., 2019; McLane et al., 2019). In contrast, the TIL subpopulations associated with a
71 good response to anti-PD-1 mAb treatment are less exhausted and moderately expanded
72 in tumors (Gueguen et al., 2021). Thus, T-cell responses in which diverse tumor-reactive
73 clones expand moderately ("clonal spreading") are also expected to exert a desirable
74 antitumor effect. However, the contribution of clonal spreading to the antitumor

75 immune response has not been intensively studied.

76 T-cell clones that recognize epitopes unrelated to tumors also infiltrate the
77 tumor tissue and form medium- and low-frequency clones ("bystander" clones) (Simoni
78 et al., 2018). Thus, to assess the clonal spreading of tumor-reactive T cells, it is
79 important to distinguish the medium- and low-frequency tumor-reactive clones from
80 bystander clones. T-cell clones present in both tumor-draining lymph nodes (dLNs) and
81 tumors (dLN-tumor overlapping (OL) clones) are considered to be enriched in tumor-
82 reactive clones that are primed in the dLN and trafficked into the tumor via blood
83 circulation (Aoki et al., 2022; Chen and Mellman, 2013). Considering that the newly
84 emerged TIL clones replace exhausted clones during the anti-PD-1 therapy (Yost et al.,
85 2019), the overlapping TIL clones supplied by the dLNs seem to play a central role in
86 anti-tumor T cell responses. We have previously demonstrated that an anti-CD4
87 monoclonal antibody (anti-CD4 mAb), which exerts potent antitumor effects in mice
88 and humans by depleting $CD4^+$ cells, including Tregs, and activating tumor-reactive
89 $CD8^+$ T-cell responses (Aoki et al., 2019, 2021; Shitara et al., 2019; Ueha et al., 2015),
90 significantly increased the number and total frequency of dLN-tumor OL clones.
91 However, it was unclear whether the increase in dLN-tumor repertoire overlap was also
92 observed with PD-1 blockade and a combination of anti-CD4 and anti-PD-L1 mAbs

93 (hereafter designated as “CD4+PDL1”), which exert synergistic anti-tumor effect (Ueha
94 et al., 2015). Furthermore, it remains unclear whether this increase in the frequency of
95 dLN-tumor OL clones is due to clonal skewing or spreading.

96 Here, we performed a T-cell receptor repertoire analysis of B16F10 and Lewis
97 lung carcinoma tumor-bearing mice treated with anti-PD-L1 and anti-CD4 mAbs. By
98 analyzing the dLN-tumor OL repertoire, we demonstrated that the number of TIL clones
99 supplied by dLNs increased after anti-PD-L1 and anti-CD4 treatment owing to clonal
100 spreading rather than clonal skewing. Moreover, the greater extent of clonal spreading
101 in anti-CD4 and CD4+PDL1 combination treatment was correlated with their superior
102 anti-tumor effects.

103

104 **Results**

105 **Anti-PD-L1 and anti-CD4 treatments increased the dLN-tumor repertoire overlap**
106 **in a B16 melanoma model**

107 In our previous study, we demonstrated that anti-CD4 treatment increases the
108 total frequency of dLN-tumor OL $CD8^+$ T-cell clones (Aoki et al., 2019). To examine
109 whether the increase in the dLN-tumor repertoire overlap also occurs in anti-PD-L1
110 treatment or in CD4+PDL1 combination treatment, we analyzed the TCR repertoire of

111 B16F10 tumor-bearing mice treated with anti-PD-L1 mAb, anti-CD4 mAb, and
112 CD4+PDL1 treatments (Figure 1A). In this model, the anti-CD4 and CD4+PDL1
113 treatments caused an antitumor effect on day 13, while the anti-PD-L1 treatment did not
114 (Figure 1B and 1C). The TCR repertoire of $CD44^{hi}$ $CD8^{+}$ T cells in the dLN and $CD8^{+}$ T
115 cells in the tumor was analyzed on day 14 after tumor inoculation (Figure 1D, E). We then
116 identified the dLN-tumor OL clones and compared their total frequency among the
117 treatment groups (Figure 1F and G). The treatment with anti-CD4 mAb and CD4+PDL1
118 significantly increased the total frequency of OL clones in the dLN and tumors (Figure
119 1H and I). The anti-PD-L1 treatment significantly increased the total frequency of OL
120 clones in the tumor to a lesser extent (Figure 1I). These results suggest that both the anti-
121 PD-L1 and anti-CD4 treatments enhanced the mobilization of tumor-reactive clones in
122 the antitumor T-cell response.

123 The clonality of the TCR repertoire, which is the extent of clonal skewing in
124 tissues, are commonly evaluated to monitor the antitumor T-cell responses (Chiffelle et
125 al., 2020). In the dLN repertoire, clonality increased in the anti-CD4 and CD4+PDL1
126 groups, consistent with the increase in the dLN-tumor repertoire overlap (Figure S1A).
127 In contrast, clonality did not change in the tumor repertoire between the treatment groups
128 with different antitumor responses (Figure S1A). This suggests that in the B16 model, the

129 dLN-tumor repertoire overlap reflects the effect of immunotherapies on the tumor T-cell
130 repertoire more clearly than the commonly used clonality index.
131
132 **Clonal spreading was prominent in the dLN-tumor repertoire overlap following**
133 **anti-PD-L1 and anti-CD4 treatments**
134 Next, we examined whether the increase in the dLN-tumor repertoire overlap
135 following the anti-PD-L1 and anti-CD4 treatments was due to clonal skewing or clonal
136 spreading of the tumor-reactive clones. For this purpose, dLN-tumor OL clones were
137 categorized into "top 10 clones" or "11th-or-lower clones" according to their frequency
138 in the tumor and were considered to belong to the "oligoclonal" or "polyclonal" fraction,
139 respectively (Figure 2A and B). The total frequencies of oligoclonal and polyclonal
140 overlap, which reflect the clonal skewing and spreading, respectively, were compared
141 between the treatment groups (Figure 2C). Oligoclonal overlap tended to increase
142 following anti-PD-L1 or anti-CD4 treatment; however, the differences were not
143 statistically significant. In contrast, polyclonal overlap increased significantly in the anti-
144 PD-L1, anti-CD4, and CD4+PD-L1 groups (Figure 2D). We also classified the clones into
145 major (> 1%), intermediate (0.1%–1%), and minor clones (< 0.1%) based on their
146 frequency within the tumor and confirmed that CD4 and PD-L1 expanded the polyclonal

147 OL clones (Figure S1B and C). Similar results were observed in the Lewis lung carcinoma
148 (LLC) tumor model: the polyclonal overlap increased in the treated groups, whereas the
149 oligoclonal overlap was the same as that in the control (Figure S1D). These results
150 demonstrate that the increase in the dLN-tumor repertoire overlap was mainly due to the
151 clonal spreading of tumor-reactive T cells rather than clonal skewing.

152 To clarify the association between clonal spreading and the antitumor effects of
153 immunotherapies, we calculated the correlation between the tumor volume on day 13 and
154 the oligoclonal or polyclonal fraction of the dLN-tumor OL repertoire (Figure 2E).
155 Polyclonal overlap was more strongly correlated with the tumor volume than oligoclonal
156 overlap. A stronger correlation between the polyclonal overlap and tumor volume was
157 also observed in the LLC model (Figure S1E). These results suggest that the clonal
158 spreading of tumor-reactive T cells induced by the anti-PD-L1 and anti-CD4 treatments
159 enhances the antitumor T-cell responses, leading to therapeutic effects.

160

161 **The polyclonal fraction of the dLN-tumor OL repertoire was enriched with**
162 **progenitor-like exhausted T cells**

163 $CD8^+$ TILs display a dysfunctional state called exhaustion, which is
164 characterized by a high expression of inhibitory receptors such as PD-1 or T-cell

165 immunoglobulin and mucin-domain containing-3 (TIM-3) (McLane, Abdel-Hakeem, and
166 Wherry, 2019). Tumors contain two subsets of exhausted T cells: terminally exhausted T
167 cells are characterized by a high expression of inhibitory receptors and exhibit high tumor
168 reactivity, while progenitor exhausted T cells are characterized by improved persistence
169 and a self-renewal capacity (Thommen et al., 2018; Miller et al., 2019; Siddiqui et al.,
170 2019; Kallies, Zehn, and Utzschneider, 2020). Because progenitor exhausted T cells can
171 proliferate and generate terminally exhausted ones following PD-1 blockade, this subset
172 is thought to be essential for a durable antitumor T-cell response (Miller et al., 2019).
173 Based on these findings, we then investigated whether the progenitor exhausted cells
174 corresponded to a polyclonal fraction of the dLN-tumor OL repertoire, which reflects
175 clonal spreading.

176 To answer this question, single-cell targeted RNA sequencing and TCR
177 sequencing (scRNA/TCRseq) were performed using a BD Rhapsody system (Figure 3A).
178 $CD8^+$ TILs were collected from B16F10 tumor-bearing mice treated with anti-CD4 mAb,
179 and a library was generated for scRNA/TCRseq. Out of the 12,397 cells analyzed, paired
180 TCR sequences were detected in 10,649 cells (pairing efficiency, 85.9%). Eight clusters
181 were identified based on the single-cell gene expression profiles (Figure 3B and S2A).
182 Based on the expression levels of marker genes (Figure 3C and S2B) and the gene

183 expression signature scores (Figure 3D and S2C), we characterized these clusters as
184 "naïve (NV)-like" (#7), "progenitor exhausted" (#4 and 6), and "terminally exhausted"
185 (#0, 1, 2, 3, and 5). Among the "progenitor exhausted" clusters, cluster 4 showed an
186 intermediate level of exhaustion scores and a lower expression level of *Tcf7*, suggesting
187 an intermediate state between progenitor exhausted and terminally exhausted states
188 (Figure 3C and D). These findings were supported by the result of pseudotime analysis,
189 which revealed the trajectory from cluster 7 (NV-like) through clusters 4 and 6 (progenitor
190 exhausted) to clusters 0 and 1 (terminally exhausted) (Figure S2B). Among the
191 "terminally exhausted" clusters, cluster 2 was highly proliferative and cluster 3 was more
192 cytotoxic, according to the *Gzma* expression level and the cytotoxicity score (Figure S2C
193 and D). Moreover, cluster 5 was characterized by a high expression of interferon-
194 responsive genes, such as *Isg15* and *Mx1* (Figure 3C and S2D). The clonality of the
195 "terminally exhausted" clusters was higher than the "progenitor exhausted" and "NV-like"
196 clusters, showing that the "terminally exhausted" clusters were composed of highly
197 expanded clones (Figure S2E).

198 To compare the phenotype of the T-cell clones consisting of the oligoclonal and
199 polyclonal fractions of the dLN-tumor OL repertoire, we identified the OL clones using
200 the results of bulk TCR-seq performed on dLN $CD8^{+}$ $CD44^{high}$ T cells collected from the

201 same mouse (Figure 3A). Oligoclonal or polyclonal OL clones were projected onto a
202 uniform manifold approximation and projection (UMAP) plot (Figure 3E, left). The
203 oligoclonal and polyclonal fractions of the dLN-tumor OL repertoire contained very few
204 cells from the "NV-like" cluster (#7), which supported the tumor reactivity of the OL
205 clones. The proportion of "terminally exhausted" clusters (#0, 1, 2, 3, and 5) was over
206 50% in the oligoclonal and polyclonal overlap. At the same time, the proportion of
207 "progenitor exhausted" clusters (#4 and 6) was higher in the polyclonal fraction (4.4% in
208 the oligoclonal fraction vs. 28.5% in the polyclonal fraction; Figure 3E, right).
209 Consistently, the polyclonal fraction was predominant in the "progenitor exhausted"
210 clusters (Figure 3F and Table S1). Moreover, the genes representing the progenitor- and
211 terminally exhausted phenotypes were highly expressed in the polyclonal and oligoclonal
212 fraction, respectively (Figure S2F). At the clone level, a higher frequency of OL clones
213 in the tumor was associated with a lower score for the progenitor exhausted state and a
214 higher score for the terminally exhausted state (Figure 3G). These results demonstrate
215 that the oligoclonal OL mainly consisted of terminally exhausted T cells, while the
216 polyclonal fraction of the dLN-tumor OL repertoire was enriched in progenitor exhausted
217 T cells.
218

219 **The polyclonal fraction of the OL repertoire was dominant in the Ly108^{+} Tim-3^{-} TIL**

220 **subpopulation**

221 To confirm the results of the scRNA/TCRseq analysis in a high-throughput

222 manner, we performed bulk TCR repertoire analysis on the CD8^{+} TIL subpopulations at

223 different exhaustion stages. Using Tim-3 and Ly108 as cell surface markers for progenitor

224 and terminally exhausted T cells (Miller et al., 2019; Kallies, Zehn, and Utzschneider,

225 2020), the CD8^{+} TILs from B16F10 tumor-bearing mice treated with anti-PD-L1 and anti-

226 CD4 were sorted into PD1^{-}, PD1^{+} Ly108^{+} Tim-3^{-} ("Ly108"), PD1^{+} Ly108^{+} Tim-3^{+} ("DP"),

227 and PD1^{+} Ly108^{-} Tim-3^{+} ("Tim-3") subsets using flow cytometry (Figure 4A). Among

228 these subpopulations, T-cell exhaustion is thought to progress in the following order: PD1^{-},

229 Ly108, DP, and Tim-3 (Miller et al., 2019). We then analyzed the TCR repertoire of these

230 four TIL subsets as well as CD44^{hi} CD8^{+} T cells in the dLN. The clonality of the TCR

231 repertoire was the lowest in PD1^{-} and gradually increased in the DP and Tim-3 subsets in

232 anti-CD4-treated mice (Figure 4B). A similar tendency was observed in the anti-PDL1

233 and CD4+PDL1 groups (Figure S3A). These results show that the repertoire of the PD1^{-}

234 and Ly108 subsets was more polyclonal than that of DP and Tim-3, consistent with the

235 scRNA/TCRseq analysis results (Figure S2D).

236 Next, we attempted to verify whether the polyclonal overlap predominated in the

237 progenitor exhausted population. For this purpose, we estimated the frequency of each
238 clone in the total $CD8^+$ TILs ("pooled") by estimating the frequency within the TIL
239 subsets ($PD1^-$, Ly108, DP, and Tim-3) weighted by the total cell count of these subsets
240 (Figure 4C, example). We confirmed that the frequency of each clone in the pooled
241 repertoire, which was estimated as described previously, was correlated with the
242 frequency in the real $CD8^+$ TIL repertoire (Figure S3B). Subsequently, the OL clones in
243 the oligoclonal and polyclonal fractions were identified based on their frequency in the
244 pooled $CD8^+$ TIL repertoire (Figure 4C), and their total frequency in each T-cell subset
245 was calculated ($PD1^-$, Ly108, DP, and Tim-3). In the anti-CD4 group, the proportion of
246 the oligoclonal fraction was significantly higher in the DP and Tim-3 subsets than in the
247 $PD1^-$ and Ly108 subsets, while that of the polyclonal fraction was the highest in the Ly108
248 subset (Figure 4D). Consistently, the proportion of the polyclonal fraction surpassed that
249 of the oligoclonal fraction in Ly108 cells (Figure 4E). These results confirmed the
250 findings of the scRNA/TCRseq analysis that the oligoclonal fraction predominated
251 among terminally exhausted T cells, while the polyclonal fraction contained more
252 progenitor exhausted T cells in the dLN-tumor OL repertoire. Notably, the CD4+PDL1
253 group exhibited results similar to those of the anti-CD4 group; however, this tendency
254 was not observed in the anti-PDL1 group (Figure S3C and D). This may reflect a weaker

255 degree of clonal spreading in the anti-PDL1 group than in the anti-CD4 or CD4+PDL1
256 group.
257
258 **Enhanced priming by migratory DCs in the dLN contributed to clonal spreading**
259 **following anti-PD-L1 and anti-CD4 treatments**
260 Our results from the TCR repertoire analysis proposed that the clonal spreading
261 of tumor-reactive T cells contributed to the antitumor effect induced by anti-PD-L1 and
262 anti-CD4 treatments in the B16F10 model. As for the mechanism of clonal spreading, we
263 hypothesized that the anti-PD-L1 and anti-CD4 treatments enhanced the priming of more
264 diverse T-cell clones in the dLN. To test this hypothesis, we utilized Fscn1$^{DTR\text{-}Cre}$ knock-
265 in mice to remove the CCR7^{+} FSCN1^{+} migratory DCs in the dLN, which play a critical
266 role in inducing tumor-reactive CD8 T-cell responses in the dLN (Roberts et al., 2016;
267 Salmon et al., 2016) (Figure S4A). FSCN1 is an actin-bundling protein that promotes the
268 migration of DCs into LNs (Adams, 2004; Lamb and Tootle, 2020; Yamakita et al., 2011).
269 Since FSCN1 is expressed not only in CCR7^{+} migratory DCs but also in neurons (Lamb
270 and Tootle, 2020; Zhang et al., 2008), we inoculated B16F10 cells into FSCN1 KI bone
271 marrow chimeric mice (FSCN1 BMC). In tumor-bearing FSCN1 BMC mice, DTR was
272 weakly expressed on a part of CCR7^{+} MHC II^{+} DCs in the tumor and strongly expressed

273 on most migratory DCs in the dLN (Figure S4B). Administration of DT to these mice
274 slightly decreased the number of CCR7^{+} MHC II^{+} DCs in the tumor and completely
275 depleted migratory DCs in the dLN (Figure S4C).

276 We subjected B16F10-bearing FSCN1 BMC mice to anti-PD-L1 and anti-CD4
277 treatments, with or without DT administration (Figure 5A). Depletion of migratory DCs
278 in the dLN of DT-treated mice was confirmed on day 14 (Figure 5B-D). TCR repertoire
279 analysis revealed that the total frequency of dLN-tumor OL clones in the tumor decreased
280 in mice receiving DT in the anti-PD-L1 and CD4+PD-L1 groups (Figure 5E). The
281 oligoclonal fraction of the dLN-tumor OL repertoire was equivalent or higher in DT-
282 treated mice compared to DT-untreated mice (Figure 5F). In contrast, the polyclonal
283 fraction of the dLN-tumor OL repertoire decreased following DT administration in all
284 three treatment groups (Figure 5G). These results suggest that the anti-CD4 and anti-PD-
285 L1 antibodies enhance the priming of tumor-reactive T-cell clones by migratory DCs in
286 the dLN, leading to clonal spreading in tumor-bearing mice.

287

288 **Discussion**

289 We demonstrated that the anti-PDL1 and anti-CD4 mAb treatment increased the
290 CD8^{+} T-cell repertoire overlap in the dLN and tumor, mainly owing to clonal spreading.

291 In the B16F10 model, anti-CD4 and CD4+PD-L1 treatments exert strong antitumor
292 effects whereas anti-PD-L1 treatment alone shows a limited antitumor effect (Ueha et al.,
293 2015). In the present study, the antitumor effect of anti-CD4, anti-PD-L1, and CD4+PD-
294 L1 treatments correlated with the extent of clonal spreading. Single-cell analysis of the
295 gene expression and TCR sequences of TILs revealed that progenitor exhausted T cells,
296 which are essential for a durable antitumor response to PD-1 blockade (Miller et al., 2019;
297 Siddiqui et al., 2019; Kallies, Zehn, and Utzschneider, 2020), were enriched in a
298 polyclonal fraction of the OL repertoire, which reflected clonal spreading. Furthermore,
299 enhanced priming in the dLN by migratory DCs contributed to the clonal spreading of
300 tumor-reactive clones following anti-PD-L1 and anti-CD4 treatments. These results
301 suggest that clonal spreading induces antitumor T-cell responses by anti-PD-L1 and anti-
302 CD4 treatments in the B16 melanoma model.

303 Our finding that clonal spreading were enhanced after anti-PD-L1 and anti-CD4
304 treatments seems to contradict with many previous studies on the repertoire analysis of
305 TILs reporting an association between oligoclonal expansion and objective antitumor
306 effects following ICIs (Dovedi et al., 2017; Riaz et al., 2017; Yusko et al., 2019; Zhang et
307 al., 2020). However, these studies did not separate $CD4^+$ and $CD8^+$ TILs prior to TCR
308 sequencing. $CD8^+$ TILs exhibit higher clonality than $CD4^+$ TILs (Gueguen et al., 2021)

309 in most cases, and the clonality of the total TIL repertoire is reported to be correlated with
310 the proportion of $CD8^+$ cells (Rudqvist et al., 2018). This evidence suggests that the
311 higher clonality in these studies reflects a larger proportion of $CD8^+$ cells in TILs. Here,
312 we performed a TCR repertoire analysis of purified $CD8^+$ T cells and clarified the clonal
313 composition changes in the $CD8^+$ T-cell repertoire under immunotherapy, which was not
314 evident in previous studies.

315 TCR repertoire analysis on dLN-tumor repertoire overlap clearly demonstrated
316 that the anti-PD-L1 and anti-CD4 treatments did not increase clonal skewing but
317 enhanced the clonal spreading of tumor-reactive T cells. Notably, the increase in the
318 polyclonal fraction of the TIL repertoire following anti-PD-L1 and anti-CD4 treatments
319 was not observed when non-overlapping clones were included in the analysis. Thus, the
320 analysis of the dLN-tumor OL, which enriches the TIL clones supplied by dLNs, is
321 important for quantifying the clonal spreading of tumor-reactive T cells and evaluating
322 antitumor T cell responses.

323 scTCR analysis of TILs and bulk TCR repertoire analysis of exhausted TIL
324 subsets revealed the immunological phenotypes of the oligoclonal and polyclonal
325 fractions of the dLN-tumor OL repertoire; unfortunately, we could not analyze untreated
326 mice owing to the low density and number of $CD8^+$ TILs in the B16F10 model. Recent

327 studies on the scTCR analysis of human TILs reported that highly expanded $CD8^+$ T cell
328 clones exhibited a terminally exhausted phenotype with tumor reactivity (Clarke et al.,
329 2019; Li et al., 2019; Zhang et al., 2018). Consistent with these findings, the oligoclonal
330 fraction of the dLN-tumor OL also largely consisted of T cells with a terminally exhausted
331 phenotype and contained a small amount of progenitor exhausted T cells. Conversely, the
332 proportion of progenitor exhausted T cells in the polyclonal fraction of dLN-tumor OL
333 was higher than that in the oligoclonal fraction. In addition, Naïve-like and $PD1^-$ $CD8^+$
334 TILs with low tumor-reactivity (Oliveira et al., 2021) were enriched in the non-OL
335 repertoire but not in the polyclonal fraction of OL, as expected. Considering that
336 terminally exhausted T-cell clones inside the tumor were replaced following PD-1
337 blockade in cancer patients (Yost et al., 2019), the OL clones in the polyclonal fraction
338 may function as reserves while oligoclonal fraction may not persist for a long period.
339 Furthermore, it is also presumed that clonal spreading owing to anti-PD-L1 and anti-CD4
340 treatments enlarges the reservoir of tumor-reactive T-cell clones, which underlies the
341 robust and persistent antitumor effect.

342 One question that remained unaddressed was how the anti-PD-L1 and anti-CD4
343 treatments enhance the clonal spread of tumor-reactive T cells. We initially hypothesized
344 that the enhanced priming of tumor-reactive clones in the dLN increases the polyclonal

345 fraction of the dLN-tumor OL repertoire. Indeed, in mouse models, the activation of T
346 cells in the dLN is enhanced by anti-CD4 (Ueha et al., 2015) and anti-PD-L1 treatments
347 (Dammeijer et al., 2020). The priming of tumor-reactive T cells in the dLN is mainly
348 mediated by $CCR7^{+}$ migratory DCs, which capture tumor antigens, mature in the tumor,
349 and migrate to the dLN via lymphatics (Roberts et al., 2016; Salmon et al., 2016).
350 Migratory DCs express a higher level of PD-L1, which interacts with PD-1 on activated
351 $CD8^{+}$ T cells in the dLN (Dammeijer et al., 2020). Moreover, the anti-CD4 treatment,
352 which removes CTLA-4 expressing Tregs, may promote the priming of $CD8^{+}$ T cells by
353 increasing the expression of CD80/86 on migratory DCs in the dLN (unpublished data).
354 These observations support the possibility that clonal spreading is promoted by the
355 enhanced priming capacity of migratory DCs. In line with this, the specific depletion of
356 migratory DCs in $FSCN1^{DTR\text{-}Cre}$ KI BMC mice reduced the polyclonal fraction of the
357 dLN-tumor OL repertoire. Our results underscore the contribution of the enhanced
358 priming in the dLN to the clonal spreading of tumor-reactive clones.

359 This study had some limitations. First, we could not demonstrate the relationship
360 between the extent of clonal spreading and clinical outcomes in patients with cancer under
361 ICI treatment. This is attributable to our limited access to the dLN specimen. TCR
362 repertoire analysis on a bilateral subcutaneous tumor model, in which tumor cells are

363 inoculated bilaterally into the backs of mice, could be an alternative approach that provide
364 the evidence for a causal relationship between clonal spreading and the antitumor effect
365 of ICIs (Tsunoda et al., 2021; Zemek et al., 2020). Second, we could not analyze the
366 immunological differences between clones contributing to clonal skewing and clonal
367 spreading, including the tumor reactivity, TCR affinity, and exhaustion status. Clones in
368 oligoclonal OL, which are observed in tumor-bearing mice, regardless of the treatment,
369 are thought to exhibit higher affinity for cancer antigens and are able to expand under
370 immune checkpoints but are more prone to exhaustion. Conversely, clones in polyclonal
371 overlap, whose expansion is enhanced by ICIs, are thought to have TCRs with lower
372 affinity for cancer antigens and need more costimulatory signals for expansion
373 (Memarnejadian et al., 2017). Cloning the TCR alpha- and beta-chain pairs using scTCR
374 sequencing and generating TCR transgenic T cells of various dLN-tumor OL clones
375 would enable us to validate the features and functions of T-cell clones contributing to
376 clonal skewing or clonal spreading. Here, we defined the oligoclonal/polyclonal fraction
377 based on the rank or frequency of clones in the tumor. However, a more refined definition,
378 which incorporates the immunological features of clones, such as the exhaustion status or
379 TCR affinity, can more precisely evaluate the extent of clonal spreading and become a
380 more reliable marker for the treatment outcome.

381 In summary, our results suggest that an enhanced clonal spreading underlies the robust
382 antitumor immune responses by which anti-PD-L1 and anti-CD4 treatments. Overall, we
383 emphasize the importance of evaluating the polyclonal nature of antitumor T-cell
384 responses through TCR repertoire analysis, which provides a novel index that reflects the
385 efficacy of ICI treatments.

386

387 **Acknowledgements**

388 We would like to thank Y. Hara for advice in cell sorting, staff of RIBS animal
389 facility for supporting the maintenance of animals, member of IGT. Inc. for expert
390 technical assistance in TCR sequencing, D. Komura and S. Ishikawa for advice in data
391 analysis. We would also like to thank Editage (www.editage.com) for English language
392 editing. Figure 5A was created with BioRender.com.

393 This work was supported by the Japan Society for the Promotion of Science
394 under Grant Number 20281832 and 17929397, and by the Japan Agency for Medical
395 Research and Development (AMED) under Grant Number JP 21gm6210025,
396 22fk0310509s0101, and 22ama221306h0001.

397

398 **Author Contributions**

399 H.A., K.M., and S.U. designed research. H.A. and S.U. performed research. T.A.
400 generated mice. H.A., M.T., H.O., H.S., H.A., and S.U. processed the samples. H.A.
401 analyzed data with supports from S.S. and S.U.. H.A. and S.U. wrote the initial draft of
402 the manuscript. All the authors participated in writing the final manuscript.
403

404 **Declaration of interests**

405 H.A. reports stock for ImmunoGeneTeqs, Inc. S.U. reports advisory role for
406 ImmunoGeneTeqs, Inc; stock for ImmunoGeneTeqs, Inc, IDAC Theranostics, Inc. S.S.
407 reports advisory role for ImmunoGeneTeqs, Inc; stock for ImmunoGeneTeqs, Inc, K.M.
408 reports consulting or advisory role for Kyowa-Hakko Kirin, ImmunoGeneTeqs, Inc;
409 research funding from Kyowa-Hakko Kirin, and Ono; stock for ImmunoGeneTeqs, Inc,
410 IDAC Theranostics, Inc.
411

412 **Figures and legends**

413 **Figure 1. The dLN-tumor repertoire overlap increases following anti-PD-L1 and**
414 **anti-CD4 treatments.** (A**)** Experimental procedure. (B and C) Growth curve (B) and
415 weight (C) of the tumor. (D and E) Gating strategy for sorting the $CD8^{+}$ $CD44^{high}$ T cells
416 in the dLN (D) and the $CD8^{+}$ T cells in the tumor (E). (F) Scheme of the dLN-tumor

417 repertoire overlap analysis. (G) Representative plot of the dLN-tumor repertoire overlap

418 for each treatment group. The plot exhibits the top 20 OL clones (colored), the OL clones

419 other than the top 20 ones (dark gray), and the non-OL clones (gray). (H and I) Frequency

420 of the OL clones in the dLN (H) and the tumor (I).

421 Means ± SEM are shown (n = 6–10 per group). One-way ANOVA and Tukey's *post-hoc*

422 test were used in (B), (C), (H), and (I); *$P \leq 0.05$; ** $P \leq 0.01$; *** $P \leq 0.001$.

423

424 **Figure 2. Increase in the polyclonal fraction of the dLN-tumor OL repertoire**

425 **following anti-PD-L1 and anti-CD4 treatments.** (A and B) Flow chart (A) and

426 representative plot (B) used for defining the oligoclonal and polyclonal fractions of the

427 dLN-tumor OL repertoire. In (B), the frequency of individual clones is plotted according

428 to their rank in the tumor in descending order. The top 10 (oligoclonal fraction) and 11th

429 or lower (polyclonal fraction) OL clones are colored in red and blue, respectively. (C and

430 D) Total frequency of the oligoclonal and polyclonal fractions of the OL clones in the

431 tumor. (E) Correlation between the tumor volume and the total frequency of the

432 oligoclonal (left) or polyclonal (right) fraction of OL clones in the tumor.

433 Means are shown (n = 6–10 per group) (C); means ± SEM are shown (n = 6–10 per group).

434 One-way ANOVA and Tukey's *post-hoc* test were used in (D); Spearman correlation test

435 was used in (E); *$P \leq 0.05$; *** $P \leq 0.001$.

436

437 **Figure 3. Single-cell analysis of the dLN-tumor OL clones following anti-CD4 mAb**

438 **treatment.** (A**)** Experimental procedure. (B) Uniform manifold approximation and

439 projection (UMAP) plot of the scRNA-seq data of $CD8^+$ TILs following anti-CD4

440 treatment. (C) Violin plot showing the expression of marker genes in the T-cell subsets.

441 (D) Violin plot showing the module scores of the feature genes of progenitor (top) and

442 terminally (bottom) exhausted T cells. (E) UMAP showing the T cells in the oligoclonal

443 or polyclonal fraction of the dLN-tumor OL repertoire (left). Pie chart showing the

444 proportion of T cells in the "naïve-like" (pink) or "progenitor exhausted" (purple) clusters

445 in the oligoclonal or polyclonal fraction (right). (F) Bar chart showing the proportion of

446 the oligoclonal (red) and polyclonal (blue) fractions of the OL clones and the non-OL

447 clones (gray) in each cluster. (G) Correlation between the clone's frequency in the tumor

448 and the progenitor or terminally exhausted score of each clone. The progenitor or

449 terminally exhausted score was calculated for each cell as in (D), and the average value

450 was then calculated for each clone.

451 Pearson correlation test was used in (E); Tex: terminally exhausted; Tex int:

452 intermediately exhausted; Tex prog: progenitor exhausted; IFN resp.: IFN responding;

453 NV-like: naïve-like; Prolif.: proliferating.

454

455 **Figure 4. Oligoclonal and polyclonal fractions of the dLN-tumor OL repertoire in**

456 **CD8$^+$ TIL subsets following anti-CD4 mAb treatment. (**A) Gating strategy used for

457 sorting the PD1$^-$, Ly108, DP, and Tim-3 CD8$^+$ TIL subsets in anti-CD4 treated mice. (B)

458 Clonality of the CD8$^+$ TIL subsets. (C) Example of the estimation of clone frequency in

459 pooled CD8$^+$ TILs based on the frequencies in each CD8$^+$ TIL subset. (D) Frequency of

460 the oligoclonal (red) or polyclonal (blue) fraction of OL clones in the CD8$^+$ TIL subsets.

461 Lines indicate the data from the same mice. (E) Bar chart showing the proportion of the

462 oligoclonal (red) or polyclonal (blue) fraction of the OL clones in each CD8$^+$ TIL subset.

463 Mean ± SEM is shown in (B) and the mean is shown in (E) (n = 5 per group) (B); one-

464 way RM ANOVA and Tukey's *post-hoc* test were used in (B) and (D); paired t-test was

465 used in (E); *$P \leq 0.05$; ** $P \leq 0.01$.

466

467 **Figure 5. Decrease in the polyclonal fraction of the dLN-tumor OL repertoire by**

468 **depleting migratory DCs following anti-PD-L1 and anti-CD4 treatments.** (A)

469 Experimental procedure. (B and C) Representative flow cytometry plot of the dLN

470 lineage$^-$ cells for CCR7$^+$ CD11c^{int} (B) and CCR7$^+$ DTR$^+$ (C) migratory DCs (migDCs) in

untreated or DT-treated mice on day 14. (D) Comparison of the frequency of $CCR7^{+}$ $CD11c^{int}$ migDCs in dLN between DT-treated and untreated mice. (E) Comparison of the frequency of OL clones in the tumor between DT-treated and untreated mice. (F and G) Comparison of the frequency of the oligoclonal (F) and polyclonal (G) fraction of dLN-tumor OL clones in the tumor between DT-treated and untreated mice.

Figure 5A was created using BioRender.com; means ± SEM are shown (n = 4–5 per group); multiple unpaired t-tests were used in (D), (E), (F) and (G); *$P \leq 0.05$; ** $P \leq 0.01$; *** $P \leq 0.001$.

STAR Methods

RESOURCE AVAILABILITY

Lead contact

Further information and requests for resources and reagents should be directed to and will be fulfilled by the lead contact, Satoshi Ueha (ueha@rs.tus.ac.jp).

Materials availability

The Fscn1 knockin mouse (Accession No. CDB0153E: https://large.riken.jp/distribution/mutant-list.html) will be distributed upon requests.

Data and code availability

489 All sequencing data (Bulk TCRseq, and Single-cell RNA/TCR sequencing) have been
490 deposited at GEO and are publicly available as of the date of publication. The accession
491 number is listed in the key resources table.
492 All original code has been deposited at Github. The link is listed in the key resources
493 table.
494 Any additional information required to reanalyze the data reported in this paper is
495 available from the lead contact upon request.

496 **EXPERIMENTAL MODEL AND SUBJECT DETAILS**

497 **Mice**

498 Eight-week-old female C57BL/6 mice (CD90.2) were purchased from Sankyo
499 Labo service corporation inc. CD90.1 congenic mice with gp100 melanoma antigen-
500 specific Pmel-1 TCR transgene (Pmel Tg) were purchased from The Jackson Laboratory,
501 then B6 mice were backcrossed for at least 6 generations. Female Pmel Tg mice were
502 used for the experiment at 8-10 weeks old. All mice were bred at specific pathogen-free
503 facilities in Research Institute for Biomedical Sciences, the Tokyo University of Science
504 and in RIKEN Kobe branch.

505 **Cell lines**

506 Lewis lung carcinoma (LLC) was kindly provided by Dr. Fuminori Abe (Nippon

507 Kayaku). B16F10 is a gp100^{+} spontaneous murine melanoma cell line, kindly provided
508 by Dr. N. Restifo (National Cancer Institute, MD). Both cell lines were cultured in RPMI-
509 1640 medium (Nakarai) supplemented with 10% fetal bovine serum (MP Bio Japan), 1%
510 HEPES (Nakarai) and 1% penicillin/streptomycin (Nakarai) at 37˚C in a humidified
511 atmosphere at 5% CO_2.

512 **Generation of Fscn1DTR-Cre knock-in mice**

513 The Fscn1 knockin mouse (Accession No. CDB0153E:
514 https://large.riken.jp/distribution/mutant-list.html) was generated by CRISPR/Cas9-
515 mediated knockin in zygotes as previously described (Abe et al., 2020). For the
516 homologous recombination-mediated knockin, the donor vector consisting of homology
517 arms and P2A-DTR-P2A-Cre (insert gene) was generated to insert the P2A-DTR-P2A-
518 Cre cassette at the 3-base upstream of the PAM sequence. For microinjection, the mixture
519 of crRNA (CRISPR RNA) (50ng/ul), tracrRNA (trans-activating crRNA) (100ng/ul),
520 donor vector (10ng/ul) and TrueCut™ Cas9 Protein v2 (100ng/ul, ThermoFisher) were
521 injected into the pronucleus of one-cell stage zygote from C57BL/6 mice. From 233
522 zygotes, 57 F0 mice were obtained and 3 of them were knockin mice confirmed by PCR,
523 in which the PCR fragments of KI allele with 5'FW and 5'REV primers (1301 bp), and
524 3'FW and 3'REV primers (587 bp) were detected (Figure S4A). The germline

525 transmissions of knockin F0 mice were confirmed by genotyping of F1 mice.

526 **Generation of BM chimeric mice**

527 Recipient B6 mice were lethally irradiated (8.5 Gy, split into 2 doses given 3

528 hours apart) the day before transplantation with 3×10^6 Fscn1-KI BM cells. Mice were

529 used for the experiments at least 8 weeks after transplantation.

530 **In vivo treatment**

531 B16F10 or LLC cells (5×10^5 cells except for Figure S3B: 2×10^5 cells) were

532 inoculated subcutaneously (s.c.) into the right flanks of C57BL/6 or Fscn1-KI BMC mice.

533 Anti-PD-L1 mAb (clone 10F.9G2, BioLegend) or Anti-CD4 mAb (clone GK1.5,

534 BioLegend) was injected intraperitoneally (i.p.) at a dose of 200 μg per mouse on days 5

535 and 9 after tumor inoculation. DT (FUJIFILM Wako) was injected intraperitoneally (i.p.)

536 at a dose of 25 ng/g continuous every second day until day 5. Tumor diameter was

537 measured twice weekly and used to calculate tumor volume (mm^3) [(major axis; mm) x

538 (minor axis; $mm)^2$]. All animal experiments were conducted in accordance with

539 institutional guidelines with the approval of the Animal Care and Use Committee of the

540 Tokyo University of Science.

541 **METHOD DETAILS**

542 **Tissue collection**

543 Intravascular leukocytes were stained by i.v. injection of FITC-conjugated mAb
544 (3 μg/mouse) against CD45.2 three minutes before sacrifice (Anderson et al., 2015).
545 Tumors and dLNs (right brachial lymph node) were collected.

546 **Preparing single cell suspension from dLN**

547 dLN cells were prepared by standard method except for Figure 5, in which dLN
548 was digested for 45 minutes at 37°C with 0.1% collagenase (FUJIFILM Wako) then
549 subjected to 25% Percoll PLUS (Cyvita) gradient and leukocytes were recovered from
550 the pellet. Lineage (CD11b, B220, NK1.1, Ter119) positive cells were depleted using BD
551 IMag Streptavidin Particles Plus-DM (BD Biosciences).

552 The cell concentration of the suspensions was determined using Flow-Count
553 fluorospheres (Beckman Coulter) and a Cytoflex flow cytometer (Beckman Coulter).
554 Cells were then stained with a mix of Fc Block (anti-mouse CD16/CD32 mAb; clone
555 2.4G2, BioLegend) and fluorophore-conjugated anti-mouse mAbs.

556 **Preparing single cell suspension from tumor**

557 Tumors were cut into small fragments and digested for 45 minutes at 37°C with
558 0.1% collagenase (FUJIFILM Wako) in Figure 1,2,4,5, and 0.1mg/mL Liberase TM
559 (Roche) in Figure 3. The cells were then subjected to 40% Percoll PLUS (Cytiva) and
560 Histopaque-1083 (Sigma-Aldrich) density separation and leukocytes were recovered

561 from the interphase. The cell concentration of the suspensions was determined using
562 Flow-Count fluorospheres (Beckman) and a Cytoflex flow cytometer (Beckman). Cells
563 were then stained with a mix of Fc Block and fluorophore-conjugated anti-mouse mAbs.
564 TCRβ^+ T cells were enriched magnetically using Anti-APC MicroBeads (Miltenyi) and
565 LS columns (Miltenyi) except for single-cell RNA/TCRseq experiment (Figure 3). In
566 single-cell RNA/TCRseq experiment, cells were stained with Sample Tag
567 oligonucleotide-conjugated antibodies in Single-Cell Multiplexing Kit (BD Biosciences)
568 as in Table S2.

569 **Flow cytometry and cell sorting**

570 CD8$^+$ (Figure 1, 2, 3, 5), CD8$^+$ PD1$^-$, CD8$^+$ PD1$^+$ Ly108$^+$ Tim3$^-$, CD8$^+$ PD1$^+$
571 Ly108$^+$ Tim3$^+$, and CD8$^+$ PD1$^+$ Ly108$^-$ Tim3$^+$ T cells (Figure 4) from tumor, and CD8$^+$
572 CD44^{high} T cells from dLN were sorted using FACS Aria II or Aria III (BD Biosciences).
573 Nonviable cells were excluded from the analysis based on forward and side scatter
574 profiles and propidium iodide staining. Intravascular leukocytes were also excluded.
575 Purity of sorted cells was always over 95%. Data were analyzed using FlowJo software
576 (version 10.8.1; BD Biosciences).

577 **TCR library construction and sequencing**

578 <u>For Figure 1, 2, and 4</u>

579 TCR sequencing libraries for next-generation sequencing were prepared
580 according to the previous report (Aoki et al., 2021). PolyA RNAs were isolated and
581 amplified from sorted T cells according to a previous report (GSE110711; Shichino et
582 al., 2019). To amplify the TCR cDNA containing complementarity determining region 3
583 (CDR3), nested PCR of the TCR locus was performed as follows. Beads containing
584 cDNA was resuspended with the 12.5 μL of first PCR mixture comprised 0.5 μL of 10
585 μM trP1 primer, and 1 μL of TCR primer mix (Trac_ex, and Trbc_ex), 4.75 μL of water,
586 and 6.25 μL of KAPA Hifi Hotstart ReadyMix (KAPA Biosystems). The thermal cycling
587 conditions were programmed as follows: denaturation at 95°C for 3 minutes, 5 cycles of
588 denaturation for 20 seconds at 98°C, annealing for 15 seconds at 65°C and extension for
589 30 seconds at 72°C, followed by a final extension at 72°C for 2 minutes. Next, 2.5 μL of
590 the first-PCR products were added into the 22.5 μL of second PCR mixture consisted of
591 1.75 μL of 10 μM primer mix (trP1, Trac_in-Bio, and Trbc_in-Bio), 8.25 μL of water
592 and 12.5 μL of KAPA Hifi Hotstart ReadyMix. The thermal cycling conditions were the
593 same as the first PCR except for the cycle number, which was 25 cycles. Next, 25 μL of
594 the second-PCR products were purified using AMPure XP (Beckman-Coulter) at a 0.7:1
595 ratio (beads−to-sample) and eluted in 20 μL of 10mM of Tris HCl pH 8.0.
596 Fragmentasion and adaptor ligation were performed using 10-20ng of second-PCR

597 product as a template with NEBNext Ultra II FS DNA Library Prep Kit for Illumina
598 (New England Biolabs) with some modifications: NEBNext Adaptor for Illumina in
599 "Adaptor Ligation" step was substituted by 5uM P1 Adaptor (duplexed), and the
600 reaction volume was 1/4 of the recommended in all steps. Adaptor-ligated DNA was
601 purified using AM Pure XP kit (Beckman-Coulter) at a 0.8:1 ratio (beads to sample) and
602 eluted in 20 μL of 10mM of Tris HCl pH 8.0. The third PCR was carried out using
603 barcoded primers to enrich the TCRβ cDNA flanked with sequencing adapters. The
604 third PCR mixture consisted of 1 μL of 10 μM trP1 primer, 1 μL of 10 μM IonA-BC[X]-
605 Trbc primer, 3 μL of template and 5 μL of NEBNext Ultra II Q5 Master Mix (accessory
606 of NEBNext Ultra II FS DNA Library Prep Kit). The thermal cycling conditions were
607 programmed as follows: denaturation at 98°C for 30 seconds, 10 cycles of denaturation
608 for 10 seconds at 98°C, annealing and extension for 1minute 15 seconds at 65°C,
609 followed by a final extension at 65°C for 5 minutes. The PCR product was purified and
610 subjected to size selection using AMPure XP kit (Beckman-Coulter) at a 1.0:1 ratio
611 (beads to sample) and eluted with 20 μL of Tris-HCl (pH 8.0). Amplified TCRβ libraries
612 were quantified using a KAPA SYBR Fast qPCR Kit (KAPA Biosystems) and size
613 distribution was analyzed by Microchip Electrophoresis System MultiNA (Shimadzu).
614 Final TCRβ libraries, whose lengths were 200–300 base pairs, were pooled and

615 sequenced using an Ion 540 Kit Chef, an Ion 540 Chip kit, and an Ion Genestudio S5
616 Sequencer (Thermo Fisher Scientific) according to the manufacturer's instructions,
617 except the flow number (500).

618 For Figure 5

619 TCR sequencing libraries for next-generation sequencing were prepared
620 according to the previous report (Tsunoda et al., 2021). In brief, mRNA in T-cell lysate
621 was captured by 10 μL of Dynabeads M270 streptavidin (Thermo Fisher Scientific)
622 bound to 2.5 pmol of BioEcoP-dT25-adapter primers. To perform reverse transcription
623 and template-switching, mRNA-trapped beads were suspended in 10 μL of RT mix [1×
624 First Strand buffer (Thermo Fisher Scientific), 1 mM dNTP (Roche), 2.5 mM DTT
625 (Thermo Fisher Scientific), 1 M betaine (Sigma-Aldrich), 9 mM MgCl2 (NIPPON
626 GENE), 1 U/μL RNaseIn Plus RNase Inhibitor (Promega), 10 U/μL Superscript II
627 (Thermo Fisher Scientific), and 1 μM of i5-TSO], and incubated for 60 min at 42ºC and
628 immediately cooled on ice. To amplify the TCR cDNA containing complementarity
629 determining region 3 (CDR3), nested PCR of the TCR locus was performed following
630 the purification of PCR product by an AM Pure XP kit (Beckman Coulter) at a 0.7:1
631 ratio of beads to sample and eluted with 20 μL of 10 mM Tris-HCl (pH 8.0). To amplify
632 TCR libraries and add adaptor sequences for the next-generation sequencer, the third

633 PCR was performed. The third-PCR products were purified as second PCR. The
634 products were pooled and then purified and subjected to dual size selection using
635 ProNex size-selective purification system (Promega) and eluted with 25 μL of 10 mM
636 Tris-HCl (pH 8.5). Final TCR libraries, whose lengths were about 600 base pairs were
637 sequenced using an Illumina Novaseq 6000 S4 flowcell (67 bp read 1 and 140 bp read
638 2) (Illumina). Only read2 contained the sequence regarding the definition of T cell
639 clones.

640 **Library preparation and sequencing for scRNA/TCRseq**

641 T cells from the spleen of Pmel Tg mouse, which stained with Single-Cell
642 Multiplexing Kit (BD Biosciences) as in Table S2, were spiked in after cell sorting. Live
643 cells were stained with Calcein AM (Nacalai) and counted using Flow-Count
644 fluorospheres (Beckman) and a Cytoflex flow cytometer (Beckman). About 18,000
645 labeled cells were trapped and reverse-transcribed using the BD Rhapsody™ (BD),
646 Targeted mRNA and AbSeq Amplification Kit (BD), and Immune Response Panel Mm
647 (BD) according to the manufacturer's instructions. Targeted mRNA, TCRseq and
648 Sample Tag libraries were prepared using according to the manufacturer's instructions
649 (VDJ CDR3 and Sample Tag Library Preparation Protocol) with the following
650 modifications; (1) BD Rhapsody™ Immune Response Panel Mm with supplement panel

651 including Cmpk2, Ifi204, Ifi211, Ifit1, Ifit3, Ifit3b, Ifit3b, Isg15, Mx1, Rsad2, and
652 Usp18 were used for target mRNA amplification. (2) we used original set of primer for
653 TCR amplification as summarized in Key resources table, and performed additional
654 PCR (3rd PCR, 6 cycles) to introduce unique dual index for sequencing. (3) we used
655 ProNex Size-Selection DNA purification System (Promega) for purification of PCR
656 product. Primers used for each PCR reaction and sample-to-beads ratios for purifying
657 PCR product were summarized in Table S3. Amplified libraries were quantified using a
658 KAPA SYBR Fast qPCR Kit (KAPA Biosystems) and size distribution was analyzed by
659 Microchip Electrophoresis System MultiNA (Shimadzu). Targeted RNAseq and Sample
660 Tag libraries were sequenced on an Illumina Novaseq 6000 S4 flowcell (67 bp read 1
661 and 140 bp read 2) (Illumina) to a depth of approximately 40,000 reads and 10,000
662 reads per cell, respectively. TCRseq libraries were sequenced on an Illumina Novaseq
663 6000 SP flowcell (67 bp read 1 and 459 bp read 2) (Illumina) to a depth of
664 approximately 20,000 reads.

665 **Data processing of TCR sequencing**

666 Adapter trimming and quality filtering of sequencing data were performed by
667 using Cutadapt-3.2 (Martin, 2013) and PRINSEQ-0.20.4 (Schmieder and Edwards,
668 2011). Sequencing data were processed by MiXCR-3.0.5 (Bolotin et al., 2015). In

669 MiXCR, filtered reads were aligned to reference mouse TCR V/D/J sequences

670 registered in the international ImMunoGeneTics (IMGT) information system: -

671 vParameters.geneFeatureToAlign = VTranscript -vjAlignmentOrder = JThenV, then

672 identical sequences were assembled and grouped in clones with PCR and sequencing

673 error correlation with the following parameters: -badQualityThreshold=10, –

674 separateByV=true, --only-productive=true, –region-of-interest=CDR3. The Variable (V)

675 and Joining (J) segment of TCRs were represented in IMGT gene nomenclature.

676 List of final clones were analyzed by VDJtools-1.2.1 (Shugay et al., 2015).

677 Then, the sequencing reads of sample was normalized to the cell count in each sample

678 by "DownSample" command of VDJtools. T-cell clones were determined as TCR reads

679 with the same TCR V segment, J segment and CDR3 nucleotide sequence.

680 **Calculation of clonality of TCR repertoire**

681 The 1 - Pielou index was used to evaluate the clonality of TCR repertoire, which

682 was calculated using the formula $1 - \sum_{i=1}^{n} p_i \log_e(p_i) / \log_e(n)$, where p_i is the

683 frequency of clone *i* for a sample with *n* unique clones.

684 **Identification of OL clones in oligoclonal and polyclonal fraction**

685 dLN-tumor OL clones were identified by "JoinSamples" function in VDJtools.

686 These OL clones were ranked in order of their frequency in the tumor. OL clones that

687 ranked in top 10 were defined as oligoclonal fraction of OL repertoire, and the other OL
688 clones were defined as polyclonal fraction. In the scRNA/TCRseq analysis, OL clones
689 were defined as those whose TCRb sequence (V segment, J segment and CDR3
690 nucleotide) was identified in the repertoire of dLN $CD8^{+}$ $CD44^{high}$ T cells, the output of
691 bulk TCRseq. The oligoclonal/polyclona fraction in scTCR analysis on TILs was defined
692 based on the frequency calculated in scTCRseq analysis.

693 **Data processing of scRNAseq reads**

694 Data processing of scRNAseq reads was performed as described in Shichino et
695 al. (TAS-seq). Adapter trimming of sequencing data was performed using cutadapt 2.10
696 (Martin, 2013). Filtered cell barcode reads were annotated by Python script provided by
697 BD Biosciences with minor modification for compatibility to Python 3.7. Associated
698 cDNA reads were mapped to reference RNA using bowtie2-2.4.2 (Langmead and
699 Salzberg, 2012) by the following parameters: -p 2 --very-sensitive-local -N 1 -norc -seed
700 656565 -reorder. Then, cell barcode information of each read was added to the bowtie2-
701 mapped BAM files by the python script and pysam 0.15.4 (Li et al., 2009), and read
702 counts of each gene in each cell barcode were counted using mawk. Resultant count data
703 was converted to a single-cell gene-expression matrix file by using R-3.6.3. The inflection
704 point of the knee-plot (total read count versus the rank of the read count) was detected

705 using DropletUtils package (v1.14.1, Lun *et al.*, 2018) in R-3.6.3. Cells of which total
706 read count was over inflection point were considered as valid cells.

707 **Data processing of sample tag reads**

708 For sample tag data, adapter trimming of sequencing data was performed by
709 using cutadapt 3.4 (Martin, 2013). Filtered reads were chunked to 64 parts for parallel
710 processing by using Seqkit 0.15.0 (Shen et al., 2016). Filtered cell barcode reads were
711 annotated by Python script provided by BD with minor modification for compatible to
712 Python3.8. Associated sample tag reads were mapped to known barcode fasta by using
713 bowtie2-2.4.2 (Langmead and Salzberg, 2012) by the following parameters: -p 2 -D 50 -
714 R 20 -N 0 -L 14 -i S,1,0.75 –norc –seed 656565 –reorder –trim-to 3:40 –score-min L,-9,0
715 –mp 3,3 –np 3 –rdg 3,3.

716 Then, cell barcode information of each read were added to the bowtie2-mapped
717 BAM files, and read counts of each Tag in each cell barcode were counted by using
718 mawk. Resulted count data was converted to Tags x cells matrix file by using data.table
719 package in R 3.6.3, and top 1M cell barcodes were extracted. For assignment of each
720 tags to each cell barcodes, read counts of each tag in each valid cell barcode, which
721 defined by the cDNA matrix, were extracted from tag/cell barcode expression matrix.
722 Unassigned cell barcodes were labeled as “not-detected” cells. Then, sum of the total

723 read counts of each tags were normalized to the minimum sum count of each tags, and
724 log_2 fold-change between first most tag counts and second most tag counts within each
725 cell barcode. Each cell barcode was ranked by the fold-change ascending order, and top
726 N cells were identified as doublets (N was calculated as theoretically detectable
727 doublets calculated by the Poisson's distribution based on the number of loaded cells,
728 total Rhapsody well number, and number of tags used).

729 **scRNAseq data analysis**

730 scRNAseq data analysis was performed by using the R software package Seurat
731 v4.0.1 (Hao et al., 2021). Expression data of targeted panel genes were converted to the
732 Seurat object. Then, genes not included in the target panel and doublet or spiked-in Pmel
733 cells were excluded. Expression data was log normalized and scaled using NormalizeData
734 and ScaleData function, respectively. Principal component analysis (PCA) against all
735 genes included in target panel was performed using RunPCA (number of calculated
736 principal components (PCs) were 100), and enrichment of each PC was calculated using
737 the JackStraw and ScoreJackStraw function (num.replicate = 100), and PCs that were
738 significantly enriched ($p \leq 0.05$) were selected for clustering and dimensional reduction
739 analysis. Dimensional reduction was performed using RunUMAP. Cell clustering was
740 performed using FindNeighbors and FindClusters against the significant PCs. Marker

741 genes of each identified cluster were identified using FindAllMarkers function
742 (test.use="wilcox", min.pct=0.1, return.thresh=0.05). Cluster constituted with
743 contaminant cells determined by marker genes were excluded and the above analysis
744 procedure was repeated.

745 **Transcriptional signature analysis in scRNAseq**

746 We computed the extent to which gene signatures were expressed in cells using
747 Seurat's "AddModuleScore" function. Progenitor and terminally exhausted signature
748 genes were obtained from the dataset of Miller et al. (Miller et al., 2019). Cytotoxicity
749 and proliferation signature genes were selected according to the descriptions in BD
750 Rhapsody™ Immune Response Panel Mm (BD). Genes used for calculating signature
751 scores were summarized in Table S4.

752 **Pseudotime analysis on scRNAseq data**

753 Pseudotime analysis was performed using the Bioconductor package Slingshot
754 v2.2.0 (Street et al., 2018). We ran the analysis using significantly enriched PCs ($p \leq 0.05$)
755 after setting Cluster 7 (NV-like) as the start cluster.

756 **Data processing of scTCRseq**

757 Raw data of single-cell TCR sequencing were processed by pipeline produced
758 by ImmunoGeneTeqs, Inc.. Briefly, sequencing reads were first separated by cell barcode,

759 then adapter trimming and quality filtering of sequencing data were performed by using
760 Cutadapt (Martin, 2013). PCR and sequencing error were corrected by lighter v1.1.2
761 (Song et al., 2014) with following parameters: -newQual 25 -maxcor 4 -K 20. Error-
762 corrected sequence reads were processed by MiXCR (Bolotin et al., 2015) to generate the
763 list of TCRα or TCRβ sequences for each cell barcode, using reference mouse TCR V/D/J
764 sequences registered in the international IMGT information system with the parameters
765 summarized in Table S5. Quality filtering of cell barcodes was performed with the
766 following criteria: (1) more than 32 TCR reads were detected. (2) the proportion of the
767 most frequent TCR sequence in cell barcode was over 0.6. (3) the cell barcode was
768 annotated to the T cell cluster in scRNAseq analysis. Finally, the most frequent sequence
769 of TCRα and TCRβ was adopted and paired in each cell barcode. Identified TCRα/β
770 sequence was imported into the meta.data matrix in Seurat object of scRNAseq data based
771 on the cellular barcode identities. T-cell clones were determined as cells with the same
772 TCRα and TCRβ pair, defined by V segment, J segment and CDR3 nucleotide sequence.
773 Frequency of each clone was calculated as the proportion of cells belonging to the clone
774 in all T cells whose TCRα and TCRβ pair was assigned.

775 **Evaluating the exhaustion status of T cell clones by TCRseq on CD8$^+$ TIL subsets.**

776 To evaluate the exhaustion status of OL clones in oligoclonal and polyclonal

777 fraction, we first calculated the frequency of clones in "Pooled" $CD8^+$ TIL repertoire from

778 the repertoire of TIL subsets ($PD1^-$, Ly108, DP, and Tim-3) as the following equation:

779 $$Freq_{k\ Pooled} = \frac{\sum_i Freq_{k\ i} \times Count_i}{\sum_i Count_i},$$

780 where *Freq* means the frequency of each clone k, and *Count* means the cell count of each

781 subset i. Then, OL clones in oligoclonal and polyclonal fraction was identified based on

782 their frequency in Pooled repertoire as above. The total frequency of these clones in each

783 TIL subset was calculated, and defined as oligoclonal and polyclonal OL repertoire in

784 each TIL subset.

785 **QUANTIFICATION AND STATISTICAL ANALYSIS**

786 Statistical analyses were performed using GraphPad Prism (ver9.2.0) software

787 (GraphPad Software) except for correlation analysis in Figure 2E and 3G. One-way

788 ANOVA with Tukey's post test was run on the comparison between treatment groups.

789 Spearman correlation test was run on the correlation analysis using cor.test function in

790 Microsoft R open 4.1.1. One-way Repeated-Measures (RM) ANOVA with Tukey's post

791 test was run on the comparison between $CD8^+$ TIL subsets. Paired t test was run on the

792 comparison between the dominance of oligoclonal or polyclonal fraction of dLN-tumor

793 OL. Multiple unpaired t tests was run on the comparison between DT treated and

794 untreated mice for each treatment group. Asterisks to indicate significance corresponding

795 to the following: n.s., not significant (P>0.05), *$P \leq 0.05$, **$P \leq 0.01$, *** $P \leq 0.001$.

796

797 **Supplemental information titles and legends**

798 **Figure S1. Related to Figure 1 and 2. Increase in the polyclonal fraction of the dLN-**
799 **tumor OL repertoire following anti-PD-L1 and anti-CD4 treatments in the B16 and**
800 **LLC subcutaneous tumor models.** (A) Clonality of $CD8^+$ $CD44^{high}$ T cells in the dLN
801 (left) and $CD8^+$ T cells in the tumor (right) in a B16 model. (B) Flow chart used for
802 defining the major, middle, and minor OL clones in the tumor in a B16 model. (C) Total
803 frequency of the major, middle, and minor OL clones in the tumor in a B16 model. (D)
804 Total frequency of the oligoclonal (left) and polyclonal (right) fractions of OL clones in
805 the tumor of an LLC model. (E) Correlation between the tumor volume and the total
806 frequency of the oligoclonal (left) or polyclonal (right) fraction of OL clones in the tumor
807 in an LLC model.

808 Means ± SEM are shown (n = 6–10 per group for the B16 model and n = 3–6 per group
809 for the LLC model). One-way ANOVA and Tukey's *post-hoc* test were used in (A), (C),
810 and (D); Spearman correlation test was used in (E); $*P \leq 0.05$; $*P \leq 0.01$; $***$ $P \leq 0.001$.

811

812 **Figure S2. Related to Figure 3. Single-cell analysis of $CD8^+$ TILs following anti-CD4**
813 **mAb treatment.** (A) Expression heatmap of the top 5 marker genes for each cluster. (B)
814 Pseudotime analysis on $CD8^+$ TILs. (Top) UMAP plot representing the pseudotime of

815 each cell. (Bottom) Violin plot showing the pseudotime for each cluster. (C) Violin plot
816 showing the module scores of feature genes related to cytotoxicity (top) and proliferation
817 (bottom). (D) Feature plots showing the expression of marker genes. (E) Clonality of the
818 $CD8^+$ TIL clusters. (F) Dot plot of the marker genes for the polyclonal and oligoclonal
819 fractions of the dLN-tumor OL repertoire. The dot size represents the percentage of
820 expressing cells. The dot color represents the average expression level across cells.
821
822 **Figure S3. Related to Figure 4. Oligoclonal and polyclonal fractions of the dLN-**
823 **tumor OL repertoire in the $CD8^+$ TIL subsets following anti-PD-L1 or CD4+PDL1**
824 **treatment. (**A) Clonality of the $CD8^+$ TIL subsets following the anti-PD-L1 (left) or
825 CD4+PDL1 (right) treatment. (B) $CD8^+$ TILs, and $PD1^-$, Ly108, DP, and Tim-3 subsets
826 of the CD8+ TILs were sorted from the same tumor. The clone frequency in the CD8+
827 TIL repertoire was compared with that in the "Pooled" repertoire, which was estimated
828 from the frequency in each $CD8^+$ TIL subset, as shown in Figure 4C. (C) Frequency of
829 the oligoclonal (red) or polyclonal (blue) fraction of OL clones in the $CD8^+$ TIL subsets
830 following the anti-PD-L1 (left) or CD4+PDL1 (right) treatment. Lines indicate the data
831 from the same mice. (D) Bar chart showing the proportion of the oligoclonal (red) or
832 polyclonal (blue) fraction of OL clones in each $CD8^+$ TIL subset following the anti-PD-

833 L1 (left) or CD4+PDL1 (right) treatment.

834 Mean ± SEM is shown in (A) and the mean is shown in (D) (n = 5 per group) (B); one-

835 way RM ANOVA and Tukey's *post-hoc* test were used in (A); paired t-test was used in

836 (D); *$P \leq 0.05$; ** $P \leq 0.01$.

837

838 **Figure S4. Related to Figure 5. Depletion kinetics of migratory DCs following DT**

839 **administration to Fscn1 KI bone marrow chimeric mice.** (A) Schematic overview of

840 the *Fscn1* allele in which the P2A-DTR-P2A-Cre sequence is knocked in. (B) Gating

841 strategy used for analyzing the $CCR7^+$ DCs in the tumor (top) and migratory DCs

842 (migDCs) or resident DCs (rDCs) in the dLN (bottom). (C) Kinetics of the DC subsets

843 following DT administration. (left) The frequency of $CCR7^+$ DCs and DTR^+ $CCR7^+$ DCs

844 among $CD45^+$ cells in the tumor was plotted. (right) Frequency of migDCs, DTR^+

845 migDCs, rDCs, and DTR^+ rDCs among live cells in the dLN were plotted.

846 Figure S4A was created using BioRender.com, and the means ± SEM are shown (n = 2

847 per group).

848

849 **Table S1. Percentage of oligoclonal or polyclonal OL in each clusters determined by**

850 **SCT**

851 **Table S2. Percentage of oligoclonal or polyclonal OL in each clusters determined by**

852 **SCT**

853 **Table S3. Conditions for PCR reaction and purification in scTCR library**

854 **preparation**

855 **Table S4. Genes used for calculating signature scores**

856 **Table S5. Parameters for MiXCR to analyze single-cell TCRseq data**

857

858 **References**

859 Abe, T., Inoue, K. ichi, Furuta, Y., and Kiyonari, H. (2020). Pronuclear Microinjection

860 during S-Phase Increases the Efficiency of CRISPR-Cas9-Assisted Knockin of Large

861 DNA Donors in Mouse Zygotes. Cell Rep. *31*, May 19, doi:

862 10.1016/j.celrep.2020.107653.

863 Adams, J.C. (2004). Roles of fascin in cell adhesion and motility. Curr. Opin. Cell Biol.

864 *16*, 590–596.

865 Ahmadzadeh, M., Johnson, L.A., Heemskerk, B., Wunderlich, J.R., Dudley, M.E.,

866 White, D.E., and Rosenberg, S.A. (2009). Tumor antigen-specific CD8 T cells

867 infiltrating the tumor express high levels of PD-1 and are functionally impaired. Blood

868 *114*, 1537–1544.

869 Anderson, K.G., Mayer-barber, K., Sung, H., Beura, L., and Britnie, R. (2015). HHS
870 Public Access. *9*, 209–222.
871 Aoki, H., Ueha, S., Shichino, S., Ogiwara, H., Hashimoto, S.I., Kakimi, K., Ito, S., and
872 Matsushima, K. (2019). TCR repertoire analysis reveals mobilization of novel CD8 + T
873 cell clones into the cancer-immunity cycle following anti-CD4 antibody administration.
874 Front. Immunol. *10*, 1–13.
875 Aoki, H., Ueha, S., Shichino, S., Ogiwara, H., Shitara, K., Shimomura, M., Suzuki, T.,
876 Nakatsura, T., Yamashita, M., Kitano, S., et al. (2021). Transient depletion of CD4þ
877 cells induces remodeling of the TCR repertoire in gastrointestinal cancer. Cancer
878 Immunol. Res. *9*, 624–636.
879 Aoki, H., Shichino, S., Matsushima, K., and Ueha, S. (2022). Revealing Clonal
880 Responses of Tumor-Reactive T-Cells Through T Cell Receptor Repertoire Analysis.
881 Front. Immunol. *13*, 1–10.
882 Aversa, I., Malanga, D., Fiume, G., and Palmieri, C. (2020). Molecular T-cell repertoire
883 analysis as source of prognostic and predictive biomarkers for checkpoint blockade
884 immunotherapy. Int. J. Mol. Sci. *21*, Mar 30, doi: 10.3390/ijms21072378.
885 Bolotin, D.A., Poslavsky, S., Mitrophanov, I., Shugay, M., Mamedov, I.Z., Putintseva,
886 E. V., and Chudakov, D.M. (2015). MiXCR: Software for comprehensive adaptive

887 immunity profiling. Nat. Methods *12*, 380–381.

888 Casarrubios, M., Cruz-Bermúdez, A., Nadal, E., Insa, A., García Campelo, M. del R.,

889 Lázaro, M., Dómine, M., Majem, M., Rodríguez-Abreu, D., Martínez-Martí, A., et al.

890 (2021). Pretreatment Tissue TCR Repertoire Evenness Is Associated with Complete

891 Pathologic Response in Patients with NSCLC Receiving Neoadjuvant

892 Chemoimmunotherapy. Clin. Cancer Res. *27*, 5878-5890

893 Chen, D.S., and Mellman, I. (2013). Oncology meets immunology: The cancer-

894 immunity cycle. Immunity *39*, 1–10.

895 Chiffelle, J., Genolet, R., Perez, M.A., Coukos, G., Zoete, V., and Harari, A. (2020). T-

896 cell repertoire analysis and metrics of diversity and clonality. Curr. Opin. Biotechnol.

897 *65*, 284–295.

898 Clarke, J., Panwar, B., Madrigal, A., Singh, D., Gujar, R., Wood, O., Chee, S.J.,

899 Eschweiler, S., King, E. V., Awad, A.S., et al. (2019). Single-cell transcriptomic

900 analysis of tissue-resident memory T cells in human lung cancer. J. Exp. Med. *216*,

901 2128–2149.

902 Dammeijer, F., van Gulijk, M., Mulder, E.E., Lukkes, M., Klaase, L., van den Bosch,

903 T., van Nimwegen, M., Lau, S.P., Latupeirissa, K., Schetters, S., et al. (2020). The PD-

904 1/PD-L1-Checkpoint Restrains T cell Immunity in Tumor-Draining Lymph Nodes.

905 Cancer Cell *38*, 685-700.e8.

906 Dovedi, S.J., Cheadle, E.J., Popple, A.L., Poon, E., Morrow, M., Stewart, R., Yusko,
907 E.C., Sanders, C.M., Vignali, M., Emerson, R.O., et al. (2017). Fractionated radiation
908 therapy stimulates antitumor immunity mediated by both resident and infiltrating
909 polyclonal T-cell populations when combined with PD-1 blockade. Clin. Cancer Res.
910 *23*, 5514–5526.

911 Gros, A., Robbins, P.F., Yao, X., Li, Y.F., Turcotte, S., Tran, E., Wunderlich, J.R.,
912 Mixon, A., Farid, S., Dudley, M.E., et al. (2014). PD-1 identifies the patient-specific
913 CD8+ tumor-reactive repertoire infiltrating human tumors. J. Clin. Invest. *124*, 2246–
914 2259.

915 Gueguen, P., Metoikidou, C., Dupic, T., Lawand, M., Goudot, C., Baulande, S.,
916 Lameiras, S., Lantz, O., Girard, N., Seguin-Givelet, A., et al. (2021). Contribution of
917 resident and circulating precursors to tumor-infiltrating CD8+ T cell populations in lung
918 cancer. Sci. Immunol. *6*, Jan 29, doi: 10.1126/sciimmunol.abd5778.

919 Hao, Y., Hao, S., Andersen-Nissen, E., Mauck, W.M., Zheng, S., Butler, A., Lee, M.J.,
920 Wilk, A.J., Darby, C., Zager, M., et al. (2021). Integrated analysis of multimodal single-
921 cell data. Cell *184*, 3573-3587.e29.

922 Havel, J.J., Chowell, D., and Chan, T.A. (2019). The evolving landscape of biomarkers

923 for checkpoint inhibitor immunotherapy. Nat. Rev. Cancer *19*, 133–150.

924 Huang, A.C., Orlowski, R.J., Xu, X., Mick, R., George, S.M., Yan, P.K., Manne, S.,
925 Kraya, A.A., Wubbenhorst, B., Dorfman, L., et al. (2019). A single dose of neoadjuvant
926 PD-1 blockade predicts clinical outcomes in resectable melanoma. Nat. Med. *25*, 454–
927 461.

928 Kallies, A., Zehn, D., and Utzschneider, D.T. (2020). Precursor exhausted T cells: key
929 to successful immunotherapy? Nat. Rev. Immunol. *20*, 128–136.

930 Street, K., Risso, D., Fletcher, R.B., Das, D., Ngai, J., Yosef, N., Purdom, E., and
931 Dudoit. S. (2010). Slingshot: cell lineage and pseudotime inference for single-cell
932 transcriptomics. BMC Genomics. *19:477*, 1–16.

933 Kidman, J., Principe, N., Watson, M., Lassmann, T., Holt, R.A., Nowak, A.K.,
934 Lesterhuis, W.J., Lake, R.A., and Chee, J. (2020). Characteristics of TCR Repertoire
935 Associated With Successful Immune Checkpoint Therapy Responses. Front. Immunol.
936 *11*, 1–11.

937 Lamb, M.C., and Tootle, T.L. (2020). Fascin in cell migration: More than an actin
938 bundling protein. Biology (Basel). *9*, 1–18.

939 Langmead, B., and Salzberg, S.L. (2012). Fast gapped-read alignment with Bowtie 2.
940 Nat. Methods *9*, 357–359.

941 van der Leun, A.M., Thommen, D.S., and Schumacher, T.N. (2020). CD8+ T cell states
942 in human cancer: insights from single-cell analysis. Nat. Rev. Cancer *20*, 218–232.
943 Li, H., Handsaker, B., Wysoker, A., Fennell, T., Ruan, J., Homer, N., Marth, G.,
944 Abecasis, G., and Durbin, R. (2009). The Sequence Alignment/Map format and
945 SAMtools. Bioinformatics *25*, 2078–2079.
946 Li, H., van der Leun, A.M., Yofe, I., Lubling, Y., Gelbard-Solodkin, D., van Akkooi,
947 A.C.J., van den Braber, M., Rozeman, E.A., Haanen, J.B.A.G., Blank, C.U., et al.
948 (2019). Dysfunctional CD8 T Cells Form a Proliferative, Dynamically Regulated
949 Compartment within Human Melanoma. Cell *176*, 775-789.e18.
950 Lun, A.T.L., Riesenfeld, S., Andrews, T., Dao, T.P., Gomes, T., and Marioni, J.C.
951 (2019). EmptyDrops: Distinguishing cells from empty droplets in droplet-based single-
952 cell RNA sequencing data. Genome Biol. *20*, Mar 22, doi: 10.1186/s13059-019-1662-y.
953 Martin, M. (2013). Cutadapt removes adapter sequences from high-throughput
954 sequencing reads. EMBnet.journal *17*, 10–12.
955 McLane, L.M., Abdel-Hakeem, M.S., and Wherry, E.J. (2019). CD8 T Cell Exhaustion
956 During Chronic Viral Infection and Cancer. Annu. Rev. Immunol. *37*, 457–495.
957 Memarnejadian, A., Meilleur, C.E., Shaler, C.R., Khazaie, K., Bennink, J.R., Schell,
958 T.D., and Haeryfar, S.M.M. (2017). PD-1 Blockade Promotes Epitope Spreading in

959 Anticancer CD8 + T Cell Responses by Preventing Fratricidal Death of Subdominant
960 Clones To Relieve Immunodomination . J. Immunol. *199*, 3348–3359.
961 Miller, B.C., Sen, D.R., Al Abosy, R., Bi, K., Virkud, Y. V., LaFleur, M.W., Yates,
962 K.B., Lako, A., Felt, K., Naik, G.S., et al. (2019). Subsets of exhausted CD8+ T cells
963 differentially mediate tumor control and respond to checkpoint blockade. Nat. Immunol.
964 *20*, 326–336.
965 Oliveira, G., Stromhaug, K., Klaeger, S., Kula, T., Frederick, D.T., Le, P.M., Forman,
966 J., Huang, T., Li, S., Zhang, W., et al. (2021). Phenotype, specificity and avidity of
967 antitumour CD8+ T cells in melanoma. Nature *596*, 119–125.
968 Overwijk, W.W., Theoret, M.R., Finkelstein, S.E., Surman, D.R., De Jong, L.A., Vyth-
969 Dreese, F.A., Dellemijn, T.A., Antony, P.A., Spiess, P.J., Palmer, D.C., et al. (2003).
970 Tumor regression and autoimmunity after reversal of a functionally tolerant state of
971 self-reactive CD8+ T cells. J. Exp. Med. *198*, 569–580.
972 Pasetto, A., Gros, A., Robbins, P.F., Deniger, D.C., Prickett, T.D., Matus-Nicodemos,
973 R., Douek, D.C., Howie, B., Robins, H., Parkhurst, M.R., et al. (2016). Tumor- and
974 Neoantigen-Reactive T-cell Receptors Can Be Identified Based on Their Frequency in
975 Fresh Tumor. Cancer Immunol. Res. *4*, 734–743.
976 Riaz, N., Havel, J.J., Makarov, V., Desrichard, A., Urba, W.J., Sims, J.S., Hodi, F.S.,

977 Martín-Algarra, S., Mandal, R., Sharfman, W.H., et al. (2017). Tumor and
978 Microenvironment Evolution during Immunotherapy with Nivolumab. Cell *171*, 934-
979 949.e15.
980 Ribas, A., and Wolchok, J.D. (2018). Cancer immunotherapy using checkpoint
981 blockade. Science (80-.). *359*, 1350–1355.
982 Roberts, E.W., Broz, M.L., Binnewies, M., Headley, M.B., Nelson, A.E., Wolf, D.M.,
983 Kaisho, T., Bogunovic, D., Bhardwaj, N., and Krummel, M.F. (2016). Critical Role for
984 CD103+/CD141+ Dendritic Cells Bearing CCR7 for Tumor Antigen Trafficking and
985 Priming of T Cell Immunity in Melanoma. Cancer Cell *30*, 324–336.
986 Rudqvist, N.P., Pilones, K.A., Lhuillier, C., Wennerberg, E., Sidhom, J.W., Emerson,
987 R.O., Robins, H.S., Schneck, J., Formenti, S.C., and Demaria, S. (2018). Radiotherapy
988 and CTLA-4 blockade shape the tcr repertoire of tumor-infiltrating t cells. Cancer
989 Immunol. Res. *6*, 139–150.
990 Salmon, H., Idoyaga, J., Rahman, A., Leboeuf, M., Remark, R., Jordan, S., Casanova-
991 Acebes, M., Khudoynazarova, M., Agudo, J., Tung, N., et al. (2016). Expansion and
992 Activation of CD103+ Dendritic Cell Progenitors at the Tumor Site Enhances Tumor
993 Responses to Therapeutic PD-L1 and BRAF Inhibition. Immunity *44*, 924–938.
994 Schmieder, R., and Edwards, R. (2011). Quality control and preprocessing of

995 metagenomic datasets. Bioinformatics *27*, 863–864.

996 Shen, W., Le, S., Li, Y., and Hu, F. (2016). SeqKit: A cross-platform and ultrafast

997 toolkit for FASTA/Q file manipulation. PLoS One *11*, 1–10.

998 Shichino, S., Ueha, S., Hashimoto, S., Otsuji, M., Abe, J., Tsukui, T., Deshimaru, S.,

999 Nakajima, T., Kosugi-Kanaya, M., Shand, F.H.W., et al. (2019). Transcriptome network

1000 analysis identifies protective role of the LXR/SREBP-1c axis in murine pulmonary

1001 fibrosis. JCI Insight *4*, Jan 10, doi: 10.1172/jci.insight.122163

1002 Shitara, K., Ueha, S., Shichino, S., Aoki, H., Ogiwara, H., Nakatsura, T., Suzuki, T.,

1003 Shimomura, M., Yoshikawa, T., Shoda, K., et al. (2019). First-in-human phase 1 study

1004 of IT1208, a defucosylated humanized anti-CD4 depleting antibody, in patients with

1005 advanced solid tumors. J. Immunother. Cancer *7*, 1–11.

1006 Shugay, M., Bagaev, D. V., Turchaninova, M.A., Bolotin, D.A., Britanova, O. V.,

1007 Putintseva, E. V., Pogorelyy, M. V., Nazarov, V.I., Zvyagin, I. V., Kirgizova, V.I., et al.

1008 (2015). VDJtools: Unifying Post-analysis of T Cell Receptor Repertoires. PLoS

1009 Comput. Biol. *11*, 1–16.

1010 Siddiqui, I., Schaeuble, K., Chennupati, V., Fuertes Marraco, S.A., Calderon-Copete, S.,

1011 Pais Ferreira, D., Carmona, S.J., Scarpellino, L., Gfeller, D., Pradervand, S., et al.

1012 (2019). Intratumoral Tcf1 + PD-1 + CD8 + T Cells with Stem-like Properties Promote

1013 Tumor Control in Response to Vaccination and Checkpoint Blockade Immunotherapy.
1014 Immunity *50*, 195-211.e10.
1015 Simoni, Y., Becht, E., Fehlings, M., Loh, C.Y., Koo, S.L., Teng, K.W.W., Yeong,
1016 J.P.S., Nahar, R., Zhang, T., Kared, H., et al. (2018). Bystander CD8+ T cells are
1017 abundant and phenotypically distinct in human tumour infiltrates. Nature *557*, 575–579.
1018 Song, L., Florea, L., and Langmead, B. (2014). Lighter: fast and memory-efficient
1019 sequencing error correction without counting. Genome Biol. *15*, Nov 15, doi:
1020 10.1186/s13059-014-0509-9.
1021 Street, K., Risso, D., Fletcher, R.B., Das, D., Ngai, J., Yosef, N., Purdom, E., and
1022 Dudoit, S. (2018). Slingshot: cell lineage and pseudotime inference for single-cell
1023 transcriptomics. BMC Genomics *19*, Jun 19, doi: 10.1186/s12864-018-4772-0.
1024 Thommen, D.S., Koelzer, V.H., Herzig, P., Roller, A., Trefny, M., Dimeloe, S.,
1025 Kiialainen, A., Hanhart, J., Schill, C., Hess, C., et al. (2018). A transcriptionally and
1026 functionally distinct pd-1 + cd8 + t cell pool with predictive potential in non-small-cell
1027 lung cancer treated with pd-1 blockade. Nat. Med. *24*, 994-1004.
1028 Tsunoda, M., Aoki, H., Shimizu, H., Shichino, S., Matsushima, K., and Ueha, S. (2021).
1029 Proportional Tumor Infiltration of T Cells via Circulation Duplicates the T Cell
1030 Receptor Repertoire in a Bilateral Tumor Mouse Model. Front. Immunol. *12*, 1–12.

1031 Ueha, S., Yokochi, S., Ishiwata, Y., Ogiwara, H., Chand, K., Nakajima, T., Hachiga, K.,
1032 Shichino, S., Terashima, Y., Toda, E., et al. (2015). Robust Antitumor Effects of
1033 Combined Anti-CD4-Depleting Antibody and Anti-PD-1/PD-L1 Immune Checkpoint
1034 Antibody Treatment in Mice. Cancer Immunol. Res. *3*, 631–640.
1035 Yamakita, Y., Matsumura, F., Lipscomb, M.W., Chou, P., Werlen, G., Burkhardt, J.K.,
1036 and Yamashiro, S. (2011). Fascin1 Promotes Cell Migration of Mature Dendritic Cells.
1037 J. Immunol. *186*, 2850–2859.
1038 Yost, K.E., Satpathy, A.T., Wells, D.K., Qi, Y., Wang, C., Kageyama, R., McNamara,
1039 K.L., Granja, J.M., Sarin, K.Y., Brown, R.A., et al. (2019). Clonal replacement of
1040 tumor-specific T cells following PD-1 blockade. Nat. Med. *25*, 1251–1259.
1041 Yusko, E., Vignali, M., Wilson, R.K., Mardis, E.R., Hodi, F.S., Horak, C., Chang, H.,
1042 Woods, D.M., Robins, H., and Weber, J. (2019). Association of Tumor
1043 Microenvironment T-cell Repertoire and Mutational Load with Clinical Outcome after
1044 Sequential Checkpoint Blockade in Melanoma. Cancer Immunol. Res. *7*, 458–465.
1045 Zemek, R.M., Fear, V.S., Forbes, C., de Jong, E., Casey, T.H., Boon, L., Lassmann, T.,
1046 Bosco, A., Millward, M.J., Nowak, A.K., et al. (2020). Bilateral murine tumor models
1047 for characterizing the response to immune checkpoint blockade. Nat. Protoc. *15*, 1628–
1048 1648.

1049 Zhang, F.R., Tao, L.H., Shen, Z.Y., Lv, Z., Xu, L.Y., and Li, E.M. (2008). Fascin
1050 expression in human embryonic, fetal, and normal adult tissue. J. Histochem.
1051 Cytochem. *56*, 193–199.
1052 Zhang, J., Ji, Z., Caushi, J.X., El Asmar, M., Anagnostou, V., Cottrell, T.R., Chan,
1053 H.Y., Suri, P., Guo, H., Merghoub, T., et al. (2020). Compartmental analysis of T-Cell
1054 clonal dynamics as a function of pathologic response to neoadjuvant PD-1 blockade in
1055 resectable non-small cell lung cancer. Clin. Cancer Res. *26*, 1327–1337.
1056 Zhang, L., Yu, X., Zheng, L., Zhang, Y., Li, Y., Fang, Q., Gao, R., Kang, B., Zhang, Q.,
1057 Huang, J.Y., et al. (2018). Lineage tracking reveals dynamic relationships of T cells in
1058 colorectal cancer. Nature *564*, 268–272.
1059

Figure 1

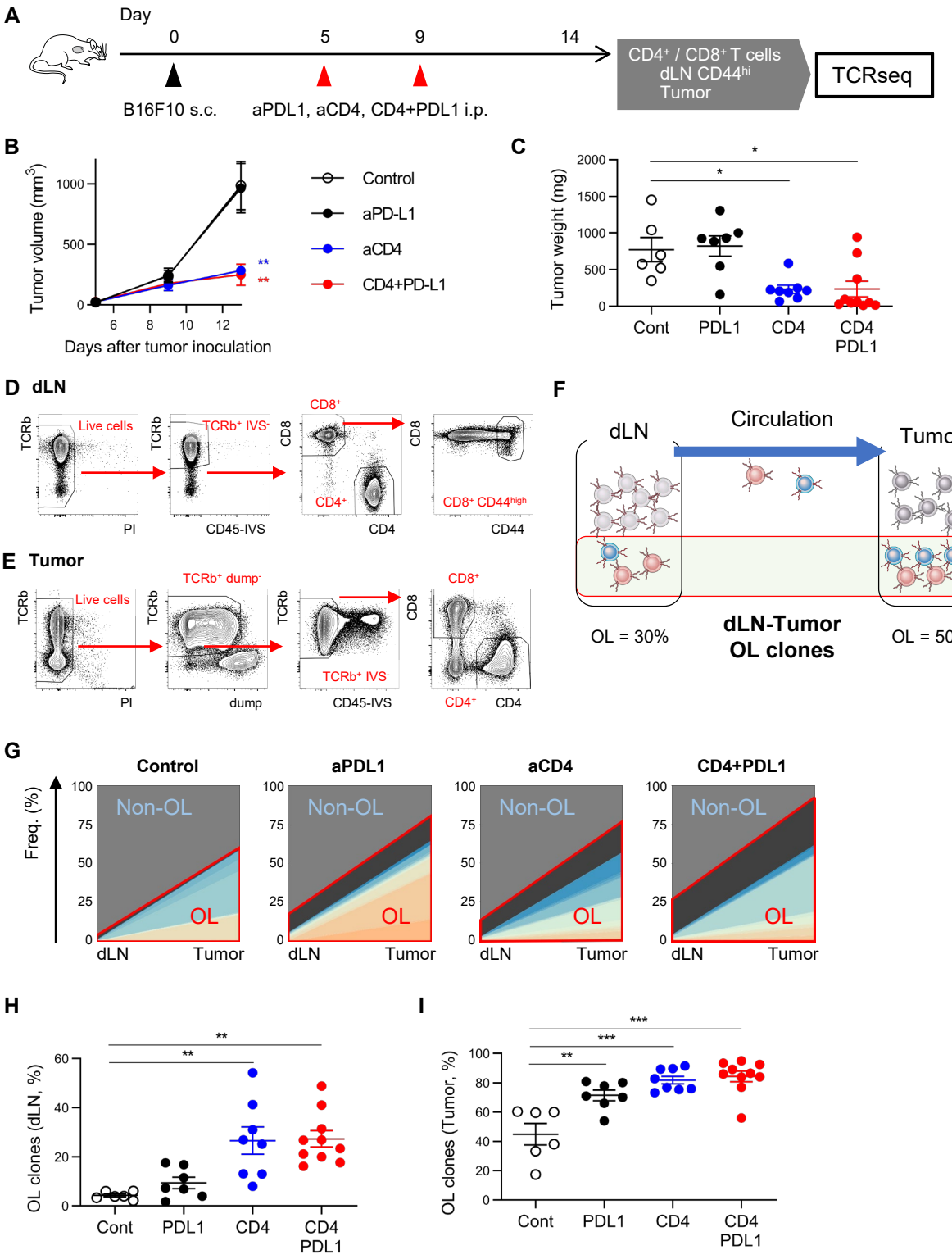
A
Day
0
5
9
14
B16F10 s.c.
aPDL1, aCD4, CD4+PDL1 i.p.
CD4+ / CD8+ T cells
dLN CD44hi
Tumor
TCRseq
B
Tumor volume (mm3)
Days after tumor inoculation
Control
aPD-L1
aCD4
CD4+PD-L1
C
Tumor weight (mg)
Cont
PDL1
CD4
CD4 PDL1
D dLN
Live cells
TCRb+ IVS-
CD8+
CD4+
CD8+ CD44high
PI
CD45-IVS
CD4
CD44
E Tumor
Live cells
TCRb+ dump-
TCRb+ IVS-
CD8+
CD4+
PI
dump
CD45-IVS
CD4
F
dLN
Circulation
Tumor
OL = 30%
dLN-Tumor
OL clones
OL = 50%
G
Control
aPDL1
aCD4
CD4+PDL1
Freq. (%)
Non-OL
OL
dLN
Tumor
H
OL clones (dLN, %)
Cont
PDL1
CD4
CD4 PDL1
I
OL clones (Tumor, %)
Cont
PDL1
CD4
CD4 PDL1

Figure 2

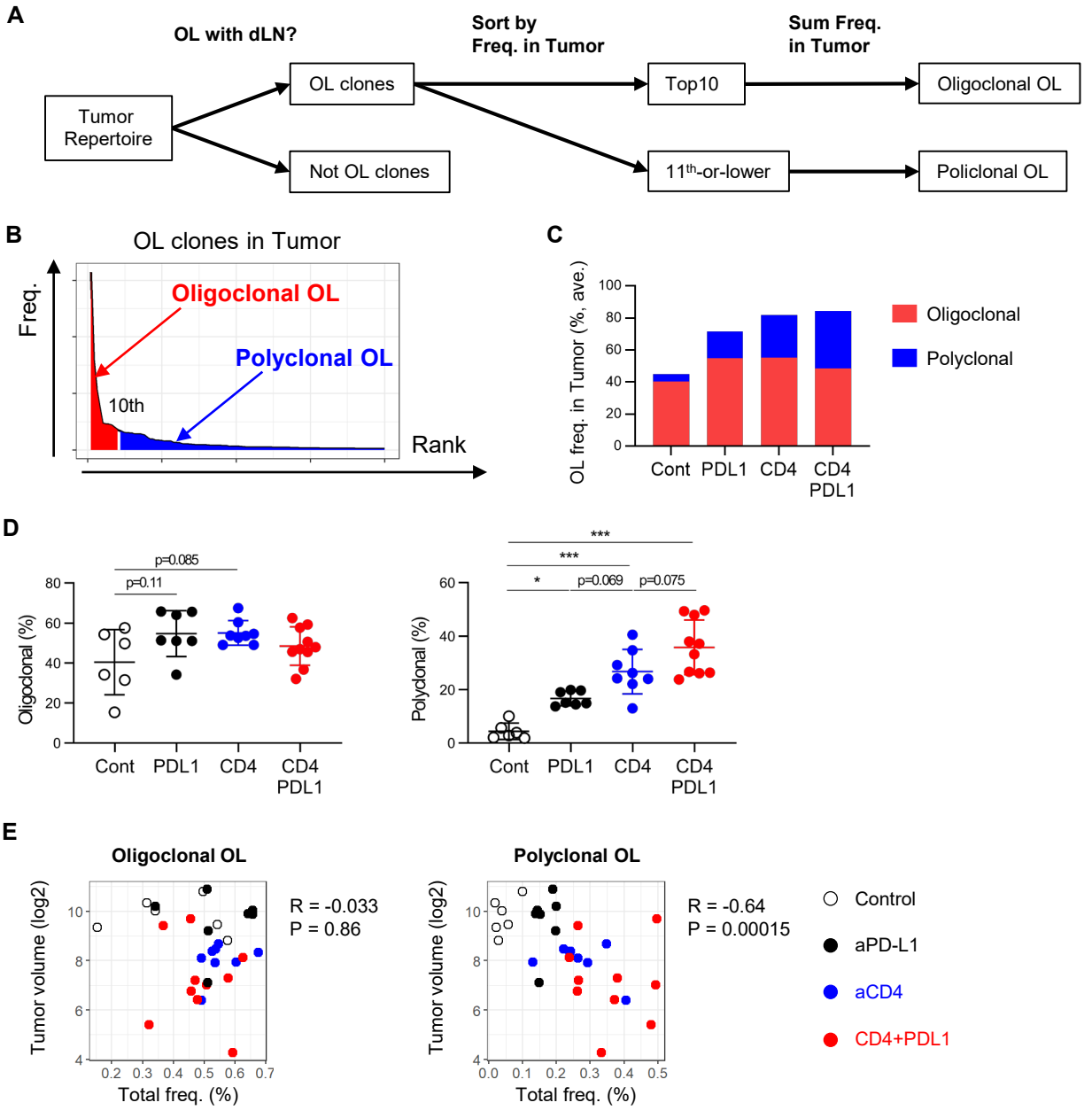
A
OL with dLN?
Sort by
Freq. in Tumor
Sum Freq.
in Tumor
Tumor
Repertoire
OL clones
Not OL clones
Top10
11th-or-lower
Oligoclonal OL
Policlonal OL
B
OL clones in Tumor
Freq.
Oligoclonal OL
Polyclonal OL
10th
Rank
C
OL freq. in Tumor (%, ave.)
Oligoclonal
Polyclonal
Cont
PDL1
CD4
CD4
PDL1
D
Oligoclonal (%)
p=0.085
p=0.11
Polyclonal (%)
***
***
*
p=0.069
p=0.075
E
Oligoclonal OL
Tumor volume (log2)
Total freq. (%)
R = -0.033
P = 0.86
Polyclonal OL
R = -0.64
P = 0.00015
Control
aPD-L1
aCD4
CD4+PDL1

Figure 3

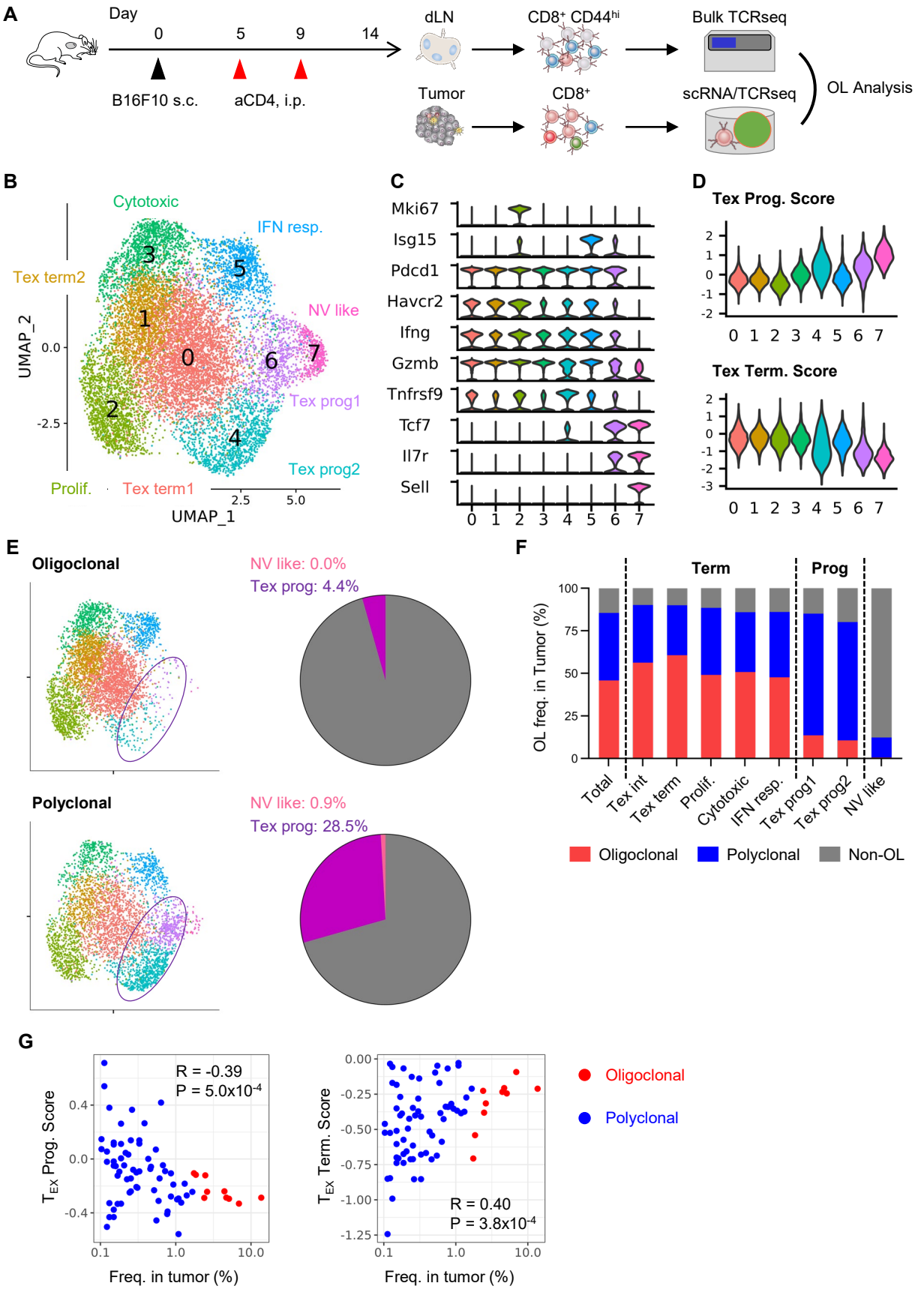
A
Day
0
5
9
14
B16F10 s.c.
aCD4, i.p.
dLN
CD8+ CD44hi
Bulk TCRseq
Tumor
CD8+
scRNA/TCRseq
OL Analysis
B
Cytotoxic
IFN resp.
Tex term2
NV like
Tex prog1
Tex prog2
Prolif.
Tex term1
UMAP_2
UMAP_1
C
Mki67
Isg15
Pdcd1
Havcr2
Ifng
Gzmb
Tnfrsf9
Tcf7
Il7r
Sell
D
Tex Prog. Score
Tex Term. Score
E
Oligoclonal
NV like: 0.0%
Tex prog: 4.4%
Polyclonal
NV like: 0.9%
Tex prog: 28.5%
F
Term
Prog
OL freq. in Tumor (%)
Total
Tex int
Tex term
Prolif.
Cytotoxic
IFN resp.
Tex prog1
Tex prog2
NV like
Oligoclonal
Polyclonal
Non-OL
G
R = -0.39
P = 5.0x10-4
TEX Prog. Score
Freq. in tumor (%)
R = 0.40
P = 3.8x10-4
TEX Term. Score
Freq. in tumor (%)
Oligoclonal
Polyclonal

Figure 4

A

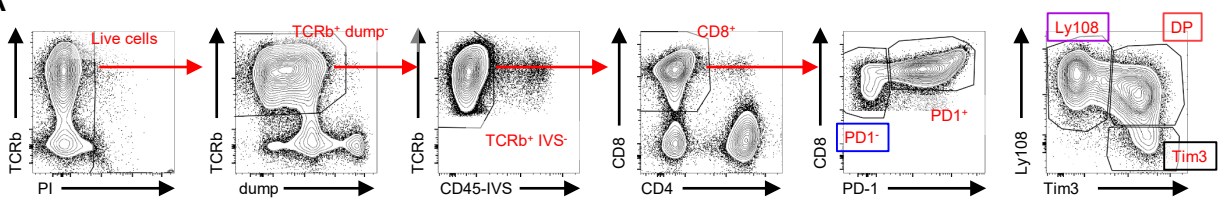

B

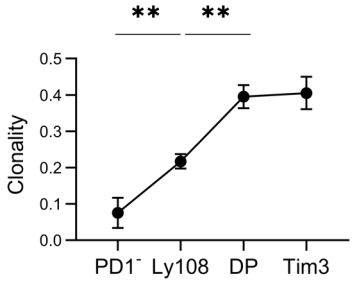

C

Subset	PD1-	Ly108	DP	Tim3	Pooled
Sorted cells	5,000	15,000	20,000	10,000	**50,000**
Freq. of clone A	0.04	0.2	0.02	0.01	**0.07**

Freq. in Pooled Tumor = (0.04 x 5000 + 0.2 x 15000 + 0.02 x 20000 + 0.01 x 10000) / 50000

D

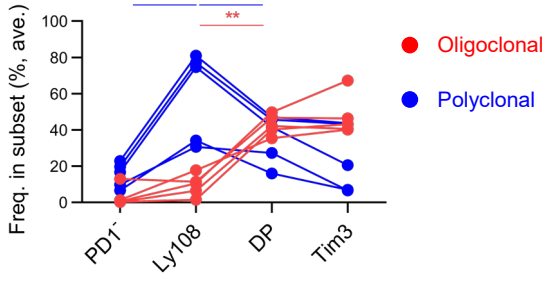

E

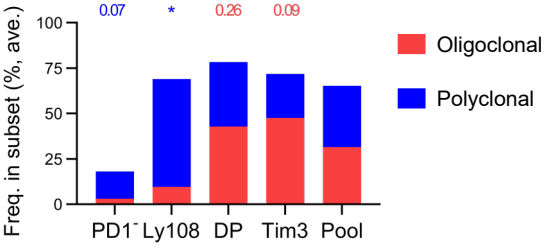

Figure 5

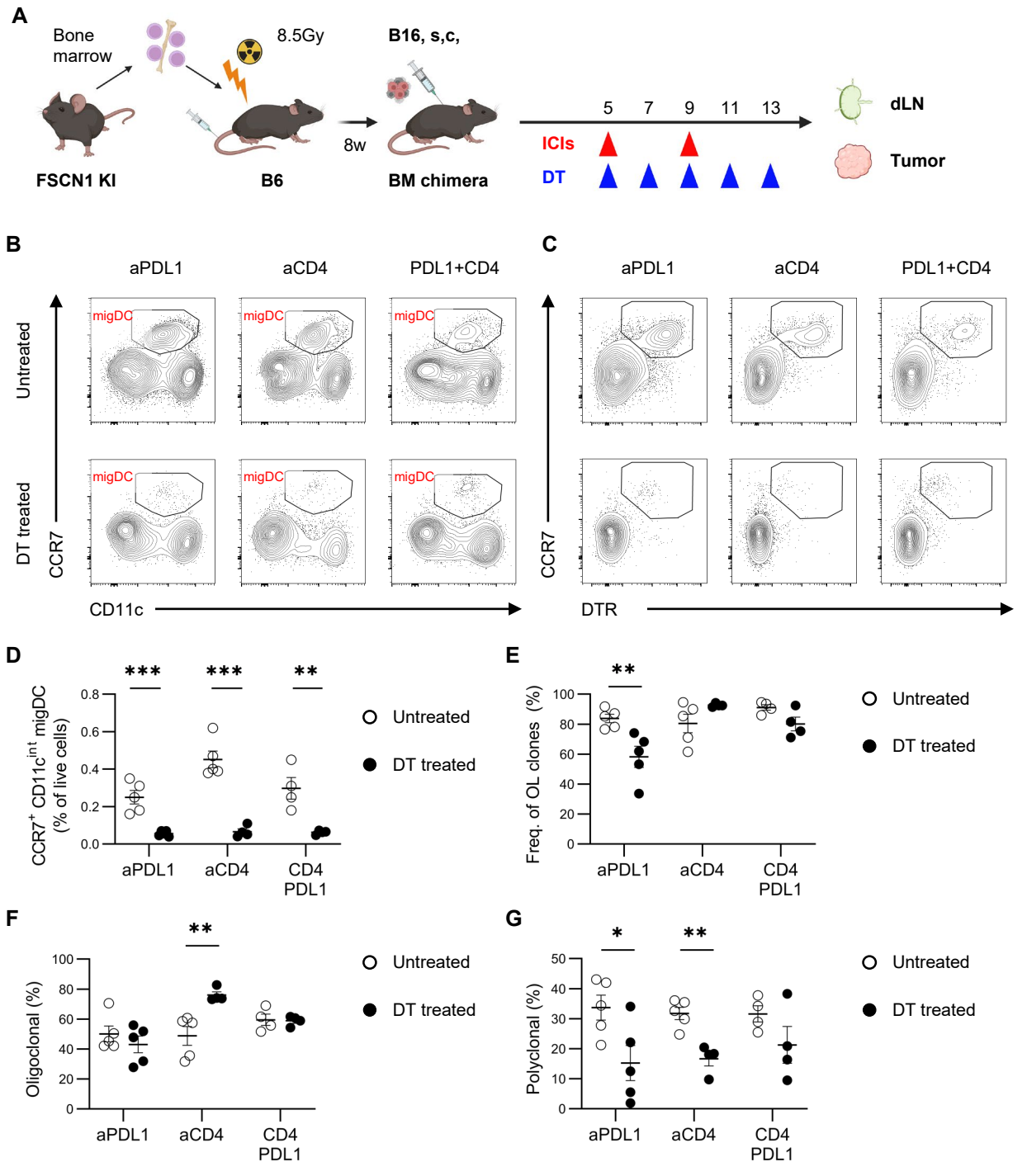
A
Bone marrow
8.5Gy
B16, s,c,
FSCN1 KI
B6
8w
BM chimera
5 7 9 11 13
ICIs
DT
dLN
Tumor
B
aPDL1
aCD4
PDL1+CD4
Untreated
DT treated
migDC
CCR7
CD11c
C
DTR
D
CCR7+ CD11c int migDC (% of live cells)
Untreated
DT treated
aPDL1
aCD4
CD4 PDL1
E
Freq. of OL clones (%)
F
Oligoclonal (%)
G
Polyclonal (%)